

RESEARCH ARTICLE

10.1002/2017JB014228

This article is a companion to Chen et al. (2017), <https://doi.org/10.1002/2017JB014226>.

Key Points:

- Microphysical constraints on the seismogenic potential (unstable slip regime) of a gouge-filled fault are presented
- Physical expressions for the critical stiffness (K_c), critical recurrence interval (W_c), and a new scaling relation of static stress drop ($\Delta\mu_s$) are provided
- A microphysical model predicts the full spectrum of fault slip behavior

Supporting Information:

- Supporting Information S1

Correspondence to:

J. Chen,
j.chen3@uu.nl

Citation:

Chen, J., & Niemeijer, A. R. (2017). Seismogenic potential of a gouge-filled fault and the criterion for its slip stability: Constraints from a microphysical model. *Journal of Geophysical Research: Solid Earth*, 122, 9658–9688. <https://doi.org/10.1002/2017JB014228>

Received 23 MAR 2017

Accepted 30 OCT 2017

Accepted article online 2 NOV 2017

Published online 4 DEC 2017

Seismogenic Potential of a Gouge-filled Fault and the Criterion for Its Slip Stability: Constraints From a Microphysical Model

Jianye Chen^{1,2}  and A. R. Niemeijer¹ 

¹HPT Laboratory, Department of Earth Sciences, Utrecht University, Utrecht, Netherlands, ²State Key Laboratory of Earthquake Dynamics, Institute of Geology, China Earthquake Administration, Beijing, China

Abstract Physical constraints for the parameters of the rate-and-state friction (RSF) laws have been mostly lacking. We presented such constraints based on a microphysical model and demonstrated the general applicability to granular fault gouges deforming under hydrothermal conditions in a companion paper. In this paper, we examine the transition velocities for contrasting frictional behavior (i.e., strengthening to weakening and vice versa) and the slip stability of the model. The model predicts a steady state friction coefficient that increases with slip rate at very low and high slip rates and decreases in between. This allows the transition velocities to be theoretically obtained and the unstable slip regime ($V_{s \rightarrow w} < V < V_{w \rightarrow s}$) to be defined. In a spring-slider configuration, linear perturbation analysis provides analytical expressions of the critical stiffness (K_c) below which unstable slip occurs and of the critical recurrence wavelength (W_c) and static stress drop ($\Delta\mu_s$) associated with self-sustained oscillations or stick slips. Numerical implementation of the model predicts frictional behavior that exhibits consecutive transitions from stable sliding, via periodic oscillations, to unstable stick slips with decreasing elastic stiffness or loading rate, and gives K_c , W_c , $\Delta\mu_s$, $V_{s \rightarrow w}$, and $V_{w \rightarrow s}$ values that are consistent with the analytical predictions. General scaling relations of these parameters given by the model are consistent with previous interpretations in the context of RSF laws and agree well with previous experiments, testifying to high validity. From these physics-based expressions that allow a more reliable extrapolation to natural conditions, we discuss the seismological implications for natural faults and present topics for future work.

1. Introduction

The classical rate- and state-dependent friction (RSF) laws were developed as a phenomenological description of frictional behavior seen in the laboratory. They have been extensively and successfully applied to natural fault mechanics, including quasi-static nucleation, slow slips, aftershock activity, and interseismic restrengthening (e.g., Ampuero & Rubin, 2008; Marone et al., 1995; Scholz, 2002). Compared with empirical friction laws, a microphysical model has the advantage of embodying the underlying physics of the friction phenomenon, allowing for a more robust extrapolation of the laboratory results to natural seismogenic conditions (e.g., Beeler, 2004; Berthoud et al., 1999; Bos & Spiers, 2002; Hatano, 2015; Ikari et al., 2016; Nakatani, 1998, 2001; Putelat et al., 2011; Sleep, 1995, 1997). Even a simplified model can be helpful provided that the underlying physical processes are constrained and described with appropriate quantitative equations and their limitations are kept in mind (e.g., den Hartog & Spiers, 2014; Niemeijer & Spiers, 2007). Recently, Chen and Spiers (2016) updated the previous model by Niemeijer and Spiers (2007), for describing the frictional behavior of a granular fault gouge undergoing deformation by granular flow accompanied by thermally activated creep and intergranular sliding at grain contacts (hereafter referred to as CNS model). We demonstrated that the model is able to reproduce typical frictional tests, namely, “velocity stepping” (VS) and “slide-hold-slide” (SHS) sequences, with modeling results in satisfactory agreement with the main features and trends seen in lab experiments (Chen et al., 2015a, 2015b). As applied to natural faults, this CNS model could provide interpretation and modeling possibilities for various fault slip phenomena, including quasi-static nucleation, stable creep, and interseismic fault healing, using appropriate kinetics-based microphysics to bridge the spatial and temporal gap between experiments and nature.

The laboratory-derived RSF laws are favored not only because they have successfully simulated many laboratory results but also because they, in combination with continuum elasticity, can explain how stable versus unstable slip can occur on natural faults (e.g., Lapusta et al., 2000; Liu & Rice, 2005, 2007; Tse & Rice, 1986).

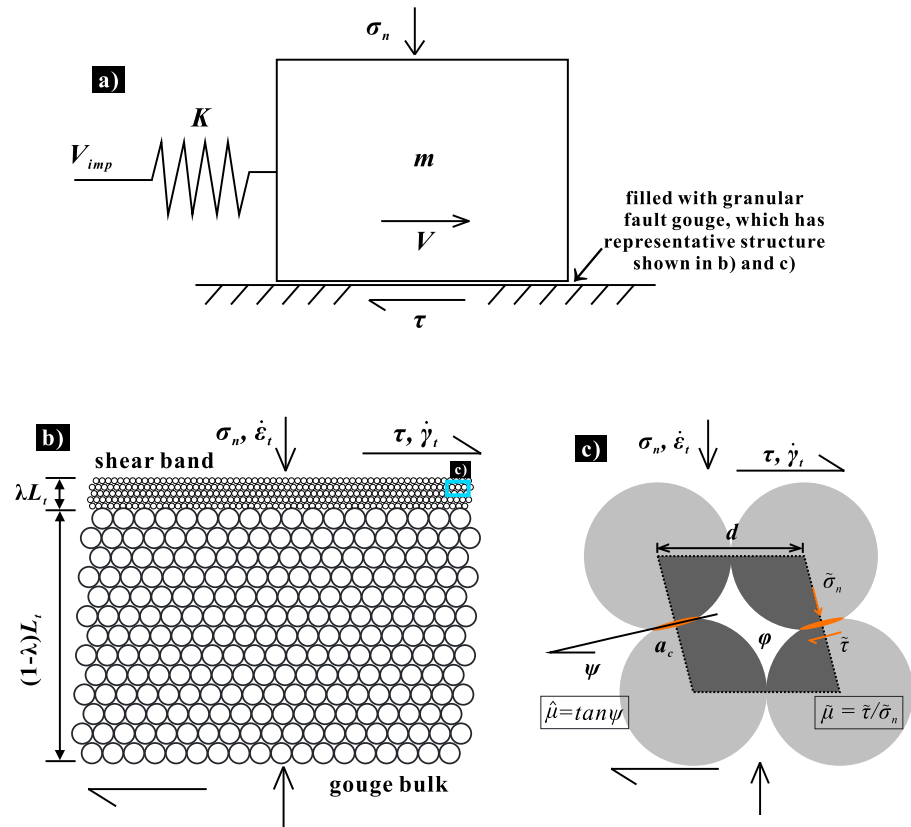


Figure 1. (a) Schematic drawing of a single degree of freedom elastic system representing a fault zone system. A slider moves along a frictional interface at a possibly varying slip rate V , which is driven by an imposed velocity V_{imp} , with stress transmitted through a spring with stiffness K . The slider mass is neglected in our analysis. In natural and laboratory fault zones, the friction interface is assumed to be filled with granular fault gouge which has an idealized (steady state) microstructure as shown in Figures 1b and 1c. (b) An idealized microstructural model for a laboratory simulated fault zone, characterized by a shear band of λL_t in thickness developed at the margin of a bulk gouge layer (L_t). The shear band is represented by densely packed spheres, with a mean diameter (d) smaller than that of the bulk layer. (c) The unit cell characterizing the grain packing in the present microstructural model, in which the key microstructural state variables, that is, porosity (ϕ), average dilatancy angle (ψ), and average contact area (a_c) are illustrated. In the model, the imposed shear deformation is accommodated by grain boundary sliding (gbs) and contact creep deformation. A cohesion-free slip criterion is used for gbs on each contact such that $\tilde{\mu} \equiv \tilde{\tau}/\tilde{\sigma}_n$, where $\tilde{\mu}$ is the gbs friction coefficient and $\tilde{\sigma}_n$ and $\tilde{\tau}$ are local normal and shear stresses acting on the contacts. The intergranular dilatancy contributes to the frictional strength by $\tan\psi$, that is, $\hat{\mu} \equiv \tan\psi$.

Episodic aseismic deformation transients (also termed slow slip events, SSEs), sometimes accompanied by low-frequency tremors (e.g., Hirose et al., 1999; Lowry et al., 2001; Wei et al., 2013, 2015) have also been explained in the framework of RSF laws by near-neutral ($a - b$) and/or small fault length scale, and/or by shear-induced dilatancy effects, as well as by introducing a cutoff velocity at high slip speeds (e.g., Hawthorne & Rubin, 2013; Liu & Rice, 2005; Segall et al., 2010; Shibasaki & Iio, 2003; Wei et al., 2015; Yoshida & Kato, 2003). It would be a marked improvement if a single microphysics-based friction law can explain the full spectrum of fault slip behavior, namely, from stable sliding, via transient slow slips, to unstable stick slips, without resorting to ad hoc constraints.

The most commonly used approach for discussing slip stability of a fault is by representing the fault zone as a spring-slider system, which represents a single-degree-of-freedom elastic system with a finite stiffness K undergoing frictional slip at its contacts with an adjoining body (Figure 1a). A simple linear stability analysis can then be applied to the fault zone with friction obeying the RSF laws with one state variable (Rice, 1983; Rice & Ruina, 1983; Linker & Dieterich, 1992). The stability criterion thus obtained reveals that steady sliding is conditionally stable when $K > K_c$ and potentially unstable when $K < K_c$, where K_c is the critical stiffness (Rice & Ruina, 1983). As K approaches K_c , the (weakly) nonlinear stability analyses further show that the slider moves

with oscillatory slip of finite amplitude (e.g., Gu et al., 1984; Putelat et al., 2010). Considering the broad consistency between RSF laws and the CNS model under stable sliding conditions ($K > K_c$), as mentioned above and in the companion paper (Chen et al., 2017, hereafter referred to as Paper 1), one may raise the question: can unstable frictional behavior be predicted by the CNS model when we perform the same linear stability analyses?

In this present paper and Paper 1, we examine the CNS model with reference to the classical works that have been done in the framework of RSF laws. In Paper 1, we obtained analytical expressions for the RSF parameters a , b , and D_c by analytically solving the constitutive equations of the CNS model. In this paper, following the works by Ruina (1983) and Dieterich and Linker (1992), we analyze the slip stability field of a spring-slider fault system, in which friction of the slider interface is governed by the CNS model. Based on the steady state shear strength profile that is inherent to the model (as addressed in Paper 1), we derive analytical expressions which constrain the potentially unstable slip regime of a seismogenic fault: ($V_{s \rightarrow w}$, $V_{w \rightarrow s}$), namely, the regime between the transition velocity from flow to friction at low slip rates and the one from velocity weakening to velocity strengthening at high slip rates. Next, we compare the results from numerical models with the analytical expressions obtained, that is, critical stiffness K_c , recurrence interval W_c , static stress drop $\Delta\mu_s$, $V_{w \rightarrow s}$, and $V_{s \rightarrow w}$. Finally, we will discuss the implications and microphysical interpretations of the application of the CNS model to natural seismogenic faults.

2. Rate- and State-Dependent Friction Laws (RSF Laws)

For frictional behavior following a rate- and state-dependent law, the shear stress (τ) is related to normal stress (σ_n), slip velocity (V), and state variable (θ) as follows (Dieterich, 1979):

$$\tau = \tau^* + a\sigma_n \ln\left(\frac{V}{V^*}\right) + b\sigma_n \ln\left(\frac{\theta}{\theta^*}\right), \quad (1)$$

where τ^* and θ^* are steady state shear stress and state variable at the reference sliding rate V^* . The evolution of the state variable is governed by either the Slowness (or Aging) law (Dieterich, 1979):

$$\dot{\theta} = 1 - \frac{V\theta}{D_c} \quad (2a)$$

or the Slip law (Ruina, 1983)

$$\dot{\theta} = -\frac{V\theta}{D_c} \ln\left(\frac{V\theta}{D_c}\right). \quad (2b)$$

The state variable (θ) is thought to represent the average lifetime of a population of grain-to-grain contacts, and D_c specifies the characteristic slip distance required to attain a new state in response to a perturbation.

The parameters in the above equations (i.e., a , b , and D_c) specify the intrinsic, material-specific frictional properties of a fault gouge. However, the frictional behavior of a fault depends not only on the frictional properties of the fault gouge but also on the elastic properties of its surroundings. For a spring-slider system, this can be described by the kinematic equation $V_{\text{imp}} = \dot{\tau}/K + V$, where V_{imp} is displacement rate at the so-called load point (i.e., the displacement rate of the spring), $\dot{\tau}$ is the time derivative of shear stress, and K is the elastic stiffness of the fault surroundings (Figure 1a). Linear perturbation analysis of such a system indicates that there exists a critical stiffness (K_c) below which any small perturbation to the steady state may grow into an instability (Rice & Ruina, 1983; Gu et al., 1984). In the context of RSF laws, the stability of a fault is controlled by K compared to K_c , which is given as $K_c = \sigma_n(b - a)/D_c$ (Ruina, 1983; Scholz, 2002). It is evident that if $(a - b) > 0$, the system is unconditionally stable under any small perturbation, responding to a steady state friction that is velocity strengthening. In contrast, if $(a - b) < 0$, the stability depends on the stiffness of the surrounding rocks and the stress on the fault and two types of behavior are possible. If $K < K_c$, the system is intrinsically unstable (Gu et al., 1984); if $K > K_c$, the system will be conditionally stable, that is, stable under a small perturbation but unstable if subjected to a sufficiently large velocity jump, such as may occur under dynamic loading in an earthquake (Scholz, 2002).

3. The Microphysical Model (CNS Model)

The CNS model is a generally applicable microphysical model for a fault gouge consisting of granular material, based on microstructural observations and inferred deformation mechanisms acting on a grain contact scale. In the model, a granular fault gouge is idealized by densely packed cylinders or spheres. Localization of slip has been taken into account, as shown in Figure 1b, by the designation of a shear band at the margin of the bulk gouge, characterized by a smaller grain size than the bulk. Such a structure has been widely observed in both natural and laboratory fault gouges (e.g., Chester et al., 1993; Verberne et al., 2013). Both gouge zones, that is, shear band and bulk sample, are characterized by the same packing, but with different mean diameters, representing the constituent particles. The frictional strength of the fault gouge is controlled by competing processes within the shear band, that is, shear-induced dilatation versus contact compaction creep for example by intergranular pressure solution (IPS). The present model only considers frictional sliding after reaching a steady state microstructure, which means that processes such as cataclasis, microcracking, and localization have not been taken into account.

The governing equations are derived by applying a unified approach to this kinematic, energy-dissipating sliding system, that is, via the conservation of momentum and energy/entropy. As given in detail by Chen and Spiers (2016), the model comprises governing equations in the original form as follows:

$$V = L_t \lambda \dot{\gamma}_{gr} + L_t \left[\lambda \dot{\gamma}_{pl}^{sb} + (1 - \lambda) \dot{\gamma}_{pl}^{bulk} \right] \quad (3a)$$

$$-\dot{\phi}^{sb} / (1 - \phi^{sb}) = \dot{\epsilon}_{pl}^{sb} - \dot{\gamma}_{gr} \tan \psi \quad (3b)$$

$$\tau = \frac{\tilde{\mu} + \tan \psi}{1 - \tilde{\mu} \tan \psi} \sigma_n \quad (3c)$$

$$\tilde{\mu} = \tilde{\mu}^* + \alpha_{\mu} \ln \left(\frac{\dot{\gamma}_{gr}}{\dot{\gamma}_{gr}^*} \right). \quad (3d)$$

In these equations, slip localization is specified by a localization degree λ and the total gouge layer thickness L_t . Superscripts “sb” and “bulk” denote the shear band and the bulk gouge, respectively. Further, $\dot{\gamma}$ and $\dot{\epsilon}$ indicate the shear and normal strain rates, respectively. Subscript “pl” indicates any nonreversible time-dependent creep mechanism at the grain contacts, acting both in the shear and normal directions, and “gr” indicates granular flow. Following these definitions, $\dot{\gamma}_{pl}^{sb}$ and $\dot{\gamma}_{pl}^{bulk}$ denote the shear strain rates by pressure solution in the shear band and bulk sample, respectively. In the present model, imposed shear displacement is assumed to be accommodated mostly by the shear band such that dilatant granular flow is negligible in the bulk which yields $\dot{\gamma}_{gr}^{bulk} = 0$ and $\dot{\gamma}_{gr} = \dot{\gamma}_{gr}^{sb}$.

The above set of equations comprises the constitutive equations of the CNS model. Equation (3a) expresses the kinematic relation in the shear direction, that is, the shear displacement rate of the sample (V) that is attributed to shear creep of the entire sample thickness and the granular flow that occurs within the shear band. Equation (3b) expresses the gouge deformation in the normal direction, where ϕ^{sb} and $\dot{\epsilon}_{pl}^{sb}$ are porosity and creep-induced compaction strain rate within the shear band, respectively. Granular flow induces dilatation, following the classical soil mechanics approach, which can be expressed using the relation $\dot{\epsilon}_{gr}^{sb} = -\dot{\gamma}_{gr} \tan \psi$ (Paterson, 1995), where the negative sign indicates dilatation and ψ is the average dilatancy angle (Figure 1c). Equation (3c) is obtained from an energy/entropy balance approach, expressing shear stress as a function of the average dilatancy angle. In doing this, we assume a cohesion-free grain boundary sliding (gbs) criterion expressed as $\tilde{\mu} = \tilde{\tau} / \tilde{\sigma}_n$ where $\tilde{\tau}$ and $\tilde{\sigma}_n$ are shear and normal stresses on the contact and $\tilde{\mu}$ is the grain boundary friction coefficient (Figure 1c). As derived from a lattice scale and based on mechanical work on an elementary energy barrier for contact sliding, gbs is intrinsically rate strengthening and can be expressed in a logarithmic form as (3d), where $\tilde{\mu}^*$ is the gbs friction coefficient at a reference strain rate $\dot{\gamma}_{gr}^*$.

Further, α_{μ} is the strain rate-dependent coefficient determined as $\alpha_{\mu} = \frac{\partial \tilde{\mu}}{\partial (\ln V)} = \frac{kT}{\sigma_l \Omega_l}$, where T is temperature, k the Boltzmann constant, Ω_l the activation volume, and σ_l the local normal stress supported by individual asperities (Chen & Spiers, 2016; see also Rice et al., 2001).

Similar to Coulomb's definition of internal friction versus internal friction angle, we define $\hat{\mu} \equiv \tan \psi$ as the dilatant friction that is required for a shearing gouge to sustain the current dilatant state, as microstructurally manifested by the dilatancy angle ψ . As such, equation (3c) can be taken as the "friction law" of the CNS model, which expresses that the frictional strength of a granular fault gouge ($\mu \equiv \tau/\sigma_n$) consists of two components, namely, grain boundary friction $\tilde{\mu}$ and friction due to intergranular dilatation $\hat{\mu}$. In the CNS model, shear band porosity (φ^{sb}), average dilatancy angle (ψ), and contact area (a_c) are referred to as the three state variables, characterizing the granular fault gouge (see their definitions in Figure 1b). Contact area a_c , which does not appear in the above equations, does play a role through affecting the creep rates ($\dot{\epsilon}_{pl}^{sb}$ and $\dot{\gamma}_{pl}$), by concentrating local stress on grain contacts or by changing the length of the diffusion path if a mass transfer process is involved. Since these variables are dependent on one another via the microstructure, the model can be idealized as a single-state-variable system once a representative microstructure is achieved (the linking functions are explained in the following). Therefore, equation (3b) can be regarded as a "state equation" of the model.

A general creep law for describing the plastic deformation at grain contacts can be written as

$$\dot{\epsilon}_{pl} \equiv E_{pl}(T, d, \sigma_n) f_{pl}(\varphi), \quad (4a)$$

where E_{pl} is a creep law for volumetric strain rate of rocks or aggregates consisting of a single mineral or mineral assemblages, which is usually expressed as a function of temperature (T), nominal grain size (d), and the applied stress (σ_n) in an exponential or power form. A porosity function $f_{pl}(\varphi)$ is introduced that accounts for changes in grain contact area (hence contact stress magnitude) as porosity evolves (Spiers et al., 2004), and we assume a general form as follows:

$$f_{pl}(\varphi) = (q - 2\varphi)^{-M}. \quad (4b)$$

Here M is the factor indicating the stress sensitivity to changes in porosity, and q is a geometrical constant, the value of which is two times the critical state porosity for granular flow ($q = 2\varphi_c$). We assume the same creep law applies anisotropically in both the shear and normal directions, as such the shear creep terms ($\dot{\gamma}_{pl}^{sb}$ and $\dot{\gamma}_{pl}^{bulk}$) can be expressed in the same form but with respect to shear stress. The average dilatancy angle and porosity can be linked by the empirical relation

$$\tan \psi = H(q - 2\varphi)^N. \quad (4c)$$

Here H is a constant representing the geometric pattern of the grains (Niemeijer & Spiers, 2007), and N is the factor indicating the sensitivity of average dilatancy angle variation with porosity. Again, q is 2 times the φ_c value, which, when $\varphi = \varphi_c$, yields the critical case at which $\tan \psi$ equals 0. See detailed explanation and possible values of these parameters in Paper 1.

3.1. Steady State Behavior of the CNS Model

As given in Paper 1, the steady state value of shear stress can be found by solving the above equations. Since the shear deformation of a sample is accommodated by two serial processes, namely, granular flow and shear creep, the steady state solutions are obtained for the two end-member cases, as given by equations (13) and (16) of Paper 1, respectively. Their combination predicts a profile of steady state shear strength showing two consecutive transitions in the rate dependence as slip rate increases (Figure 2). Consequently, three distinct steady state deformation regimes emerge:

1. At low slip rates, the deformation is fully accommodated by dilationless shear creep (flow), exhibiting strongly velocity strengthening behavior.
2. At intermediate slip rates, the deformation is mainly attributed to dilatant granular flow (slip), the dilative component of which, when a steady state is achieved, is balanced by compaction due to creep at grain contacts. This combined process is velocity weakening with a sensitivity that decreases with increasing velocity.
3. As the slip rate increases further, the dilatant effect becomes less important and the shear strength is controlled by grain boundary sliding, which is inherently velocity strengthening.

A similar trend of frictional strength varying with slip rate has been observed in experiments on rock or analogue materials such as quartz, calcite, serpentinite, halite, halite-phyllsilicate and quartz-muscovite

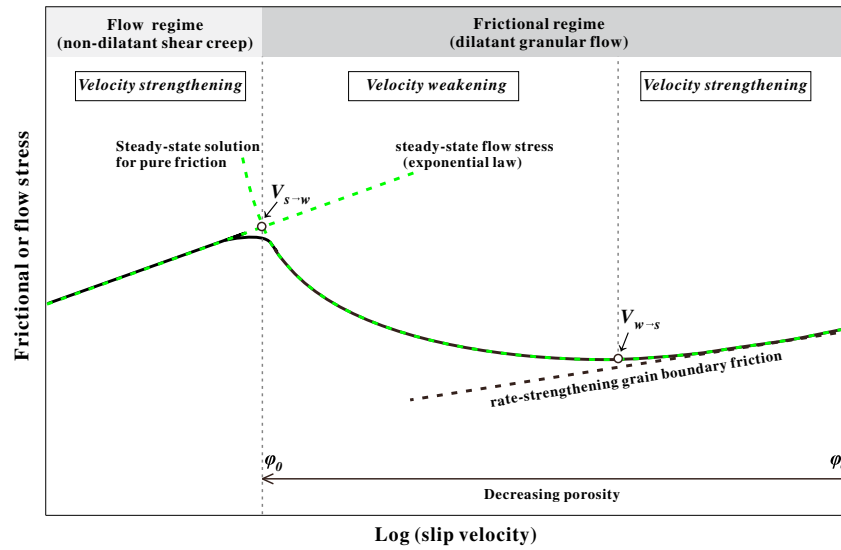


Figure 2. Schematic model of the steady state frictional or flow stress as a function of logarithmic slip velocity for a granular fault gouge. The profile indicates three deformation regimes with increasing velocity: from strengthening by pure shear creep (flow) at low velocities, via weakening at intermediate velocities, back to strengthening at velocities. Different regimes are separated by two transition velocities, $V_{s \rightarrow w}$ and $V_{w \rightarrow s}$. The entire profile is captured by the analytical solutions for the two end-member cases, namely, deformation is controlled by pure flow or pure friction.

mixtures, and natural clay-rich fault gouges (e.g., Bos & Spiers, 2002; Buijze et al., 2017; Chester & Higgs, 1992; Moore et al., 1997; Niemeijer et al., 2016; Shimamoto, 1986), mostly under hydrothermal conditions. It is appealing that different regimes of deformation from slow to high slip rates can be predicted using a single physics-based model. It is noteworthy that at even higher slip rates (>0.1 m/s), the frictional strength is expected to decrease sharply due to thermal weakening, which is not included in the present model.

3.2. (Stable) Transient Behavior of the CNS Model

To simulate transient behavior, we present the fault as a spring-slider system composed of a linear spring of stiffness K , activated by the imposition of a constant velocity at the load point (V_{imp}), assuming no inertia. In the context of this framework, equations (3a) and (3b) can then be rewritten into a pair of ordinary differential equations (ODEs), as follows:

$$\frac{1}{K} \frac{d\tau}{dt} = V_{imp} - L_t \lambda \dot{\gamma}_{gr} - \left[L_t \lambda \dot{\gamma}_{pl}^{sb} + L_t (1 - \lambda) \dot{\gamma}_{pl}^{bulk} \right] \quad (5a)$$

$$\frac{1}{(1 - \phi^{sb})} \frac{d\phi^{sb}}{dt} = \tan \psi \dot{\gamma}_{gr} - \dot{\epsilon}_{pl}^{sb} \quad (5b)$$

Combining equations (3c) and (3d) gives

$$\dot{\gamma}_{gr} = \dot{\gamma}_{gr}^* \exp \left[\frac{\tau (1 - \tilde{\mu}^* \tan \psi) - \sigma_n (\tilde{\mu}^* + \tan \psi)}{\alpha_{\mu} (\sigma_n + \tau \tan \psi)} \right] \quad (6)$$

Besides shear stress (τ) and state of the gouge (ϕ , ψ , and a_c), the parameters in the above equations fall into two categories. One is related to the fault configuration, termed as "Para.fault" and includes shear zone thickness L_t , localization degree λ , particle size d , temperature T , effective normal stress σ_n , and imposed slip velocity V_{imp} . The other category consists of the kinetic constants of the inferred deformation mechanism(s), termed as "Para.rheology." Recall that in the present model a gouge deforms by intergranular slip and creep at grain contacts. As such, the rheological category should consist of both the gbs-related parameters (e.g., $\tilde{\mu}^*$ and α_{μ}) and the creep-related parameters (e.g., activation energy, apparent activation volume, grain size exponent, stress exponent). By using all these parameters, the corresponding strain rates (i.e., $\dot{\epsilon}_{pl}^{sb}$, $\dot{\gamma}_{pl}^{sb}$, $\dot{\gamma}_{pl}^{bulk}$, and $\dot{\gamma}_{gr}$) can be expressed as functions of the macroscopic stresses (τ and σ_n) and state (ϕ) of the gouge.

Based on the above considerations, the equation set (5a) and (5b) can be rewritten as

$$\begin{aligned}\frac{d\tau}{dt} &= f(\tau, \varphi, \text{Para.fault}, \text{Para.rheology}, V_{\text{imp}}) \\ \frac{d\varphi}{dt} &= g(\tau, \varphi, \text{Para.fault}, \text{Para.rheology}).\end{aligned}\quad (7)$$

These are two equations containing two independent variables, τ and φ . To avoid complexity, we ignore the superscript sb in the following except where otherwise stated. As such, φ is referred to as shear band porosity and $\dot{\epsilon}_{\text{pl}}$ as the creep-induced compaction strain rate in the shear band. The transient behavior of a fault can, therefore, be determined by solving these two ODEs at a given boundary condition. Note that in equation (7), the imposition of load point velocity V_{imp} is set as the default boundary condition. However, the model is not inherent to a velocity boundary; any perturbation to the spring-slider system can be taken as a boundary condition. Interesting issues relevant to this include the frictional behavior of a fault in response to temporal variations in effective normal stress (σ_n), temperature (T), wall-rock stiffness (K), grain size (d), and slip (de) localization (λ).

Equation set (7) also suggests that the CNS model can be considered as a single-state-variable, rate- and state-dependent friction law, just like the classical RSF laws (Slowness and Slip laws). Using these equations, we have simulated typical velocity stepping and slide-hold-slide tests. The modeling results capture the main features and trends seen in the experiments, including both steady state and transient aspects of the observed behavior (Chen & Spiers, 2016). In Paper 1, we further showed that the frictional behavior predicted by the CNS model is consistent with the predictions by the classical RSF laws for small perturbations. Considering the consistency with the RSF laws, one may immediately raise the question: do the fault stability regimes of the RSF laws, as given above, still hold in the framework of the CNS model?

4. Linearized Stability Analysis

Under constant normal stress conditions, if the frictional strength of a system changes by a small amount and returns to a steady state when subjected to a small perturbation, the system can be considered as a linearly stable system. In this section, we examine the stability of the CNS model by performing a linear perturbation analysis following Dieterich and Linker (1992).

To make mathematics convenient, we first specify the model as follows. We take diffusion-controlled intergranular pressure solution (IPS) as the contact-scale creep mechanism, the compaction strain rate of which, corresponding to (4a), can be expressed in a linear law as

$$\dot{\epsilon}_{\text{pl}} = \frac{A_n D C S \sigma_n \Omega}{R T d^3} \frac{1}{(q - 2\varphi)^2}. \quad (8a)$$

In this equation, A_n is a geometric constant for compaction, D is the diffusivity of the solute within the grain boundary fluid (m^2/s), C is the solubility of the solid species in the solution (m^3/m^3), S is the effective thickness of the grain boundary fluid phase (m), Ω is the molar volume of the solid phase (m^3/mol), and R is the universal gas constant ($8.31 \text{ J mol}^{-1} \text{ K}^{-1}$). The last term of the above equation indicates an M value of 2, as has been theoretically derived as well as observed in experiments (Spiers et al., 2004). An empirical N value of 1 was adopted for a gogue deforming by IPS and granular flow (Niemeijer & Spiers, 2007). These generate the following relations that correspond to (4b) and (4c):

$$f_{\text{pl}}(\varphi) = (q - 2\varphi)^{-2} \quad (8b)$$

$$\tan\psi = H(q - 2\varphi). \quad (8c)$$

We consider the frictional regime in which the shear creep contributes negligibly to the imposed slip rate, as will be confirmed later by the numerical simulations. Recall that we define $\hat{\mu} \equiv \tan\psi$ as the friction due to intergranular dilatation. As such, equation (8a) can be simplified as

$$\dot{\epsilon}_{\text{pl}} = \Gamma \hat{\mu}^{-2}, \quad (9)$$

where Γ is a constant for constant σ_n , T , and d : $\Gamma = A_n H^2 DCS \sigma_n \Omega / (RTd^2)$. Without loss of generality, we set the preperurbation stable sliding as a reference ($\dot{\gamma}_{gr}^* = V_{imp}/L_t \lambda$), which yields

$$\tilde{\mu}_{ss} = \tilde{\mu}^* + a_{\mu}^{-1} \ln \left(\frac{\dot{\gamma}_{gr}}{\dot{\gamma}_{gr}^*} \right) = \tilde{\mu}^*. \quad (10a)$$

At steady state, this, combined with (9), gives $\dot{\gamma}_{gr} = \dot{\gamma}_{gr}^* = \dot{\epsilon}_{pl}/\hat{\mu}_{ss} = \Gamma(\hat{\mu}_{ss})^{-3}$. From this, we further have

$$\hat{\mu}_{ss} = (L_t \lambda \Gamma / V_{imp})^{1/3}. \quad (10b)$$

The macroscopic steady state friction coefficient can be thus calculated as

$$\mu_{ss} = \frac{\tilde{\mu}_{ss} + \hat{\mu}_{ss}}{1 - \tilde{\mu}_{ss} \hat{\mu}_{ss}}. \quad (10c)$$

Based on all the above considerations, equations (4a)–(4c), (5a), and (5b) can be respectively rewritten as

$$\frac{d\mu}{dt} = \frac{K}{\sigma_n} (V_{imp} - L_t \lambda \dot{\gamma}_{gr}) \equiv F(\mu, \hat{\mu}) \quad (11a)$$

$$\frac{d\hat{\mu}}{dt} = -2H(1 - \varphi) (\hat{\mu} \dot{\gamma}_{gr} - \Gamma \hat{\mu}^{-2}) \equiv G(\mu, \hat{\mu}) \quad (11b)$$

and

$$\dot{\gamma}_{gr} = \dot{\gamma}_{gr}^* \exp \left[\frac{\mu(1 - \tilde{\mu}_{ss} \hat{\mu}) - \sigma_n(\tilde{\mu}_{ss} + \hat{\mu})}{a_{\mu}(1 + \mu \hat{\mu})} \right]. \quad (12)$$

To perform a linear perturbation analysis, we introduce new variables to represent the departure of variables from the steady state solution:

$$\langle \mu \rangle = \mu - \mu_{ss} \text{ and } \langle \hat{\mu} \rangle = \hat{\mu} - \hat{\mu}_{ss}. \quad (13)$$

Here μ_{ss} and $\hat{\mu}_{ss}$ are the steady state solutions as given in equations (10a)–(10c) for a constant slip rate V_{imp} . The constitutive relations (11a) and (11b) are then linearized taking

$$\begin{aligned} \frac{d\langle \mu \rangle}{dt} &= \left(\frac{\partial F}{\partial \mu} \right) \langle \mu \rangle + \left(\frac{\partial F}{\partial \hat{\mu}} \right) \langle \hat{\mu} \rangle \\ \frac{d\langle \hat{\mu} \rangle}{dt} &= \left(\frac{\partial G}{\partial \mu} \right) \langle \mu \rangle + \left(\frac{\partial G}{\partial \hat{\mu}} \right) \langle \hat{\mu} \rangle. \end{aligned} \quad (14)$$

The partial derivatives in (14) are evaluated at steady state using (10a)–(10c). From then on, these partial derivatives are considered to be constant. This yields a pair of linear equations for $d\langle \mu \rangle/dt$ and $d\langle \hat{\mu} \rangle/dt$ in terms of $\langle \mu \rangle$ and $\langle \hat{\mu} \rangle$:

$$\begin{pmatrix} \frac{d\langle \mu \rangle}{dt} \\ \frac{d\langle \hat{\mu} \rangle}{dt} \end{pmatrix} = \begin{pmatrix} A_{11} & A_{12} \\ A_{21} & A_{22} \end{pmatrix} \begin{pmatrix} \langle \mu \rangle \\ \langle \hat{\mu} \rangle \end{pmatrix} = A \begin{pmatrix} \langle \mu \rangle \\ \langle \hat{\mu} \rangle \end{pmatrix} \quad (15)$$

where

$$A_{11} = \frac{\partial F}{\partial \mu} = -\frac{KL_t \lambda \dot{\gamma}_{gr}^* (1 - \tilde{\mu}_{ss} \hat{\mu}_{ss})}{\sigma_n a_{\mu}^{-1} (1 + \mu_{ss} \hat{\mu}_{ss})} = -\frac{KV_{imp} (1 - \tilde{\mu}_{ss} \hat{\mu}_{ss})^2}{\sigma_n a_{\mu}^{-1} (1 + \hat{\mu}_{ss}^2)} \quad (16a)$$

$$A_{12} = \frac{\partial F}{\partial \hat{\mu}} = \frac{L_t \lambda K \dot{\gamma}_{gr}^* \mu_{ss} \tilde{\mu}_{ss} + 1}{\sigma_n a_{\mu}^{-1} (1 + \mu_{ss} \hat{\mu}_{ss})} = \frac{KV_{imp} (1 + \tilde{\mu}_{ss}^2)}{\sigma_n a_{\mu}^{-1} (1 + \hat{\mu}_{ss}^2)} \quad (16b)$$

$$A_{21} = \frac{\partial G}{\partial \mu} = -2H(1 - \varphi_{ss}) \dot{\gamma}_{gr}^* \frac{\hat{\mu}_{ss} (1 - \tilde{\mu}_{ss} \hat{\mu}_{ss})}{a_{\mu}^{-1} (1 + \mu_{ss} \hat{\mu}_{ss})} = -\frac{2H(1 - \varphi_{ss}) V_{imp} \hat{\mu}_{ss} (1 - \tilde{\mu}_{ss} \hat{\mu}_{ss})^2}{L_t \lambda a_{\mu}^{-1} (1 + \hat{\mu}_{ss}^2)} \quad (16c)$$

$$A_{22} = \frac{\partial G}{\partial \hat{\mu}} = -6H(1 - \varphi_{ss}) \dot{\gamma}_{gr}^* \left[1 - \frac{\hat{\mu}_{ss} (\mu_{ss} \tilde{\mu}_{ss} + 1)}{3a_{\mu}^{-1} (1 + \mu_{ss} \hat{\mu}_{ss})} \right] = \frac{6H(1 - \varphi_{ss}) V_{imp}}{L_t \lambda} \left[\frac{\hat{\mu}_{ss} (1 + \tilde{\mu}_{ss}^2)}{3a_{\mu}^{-1} (1 + \hat{\mu}_{ss}^2)} - 1 \right]. \quad (16d)$$

Note that in doing the partial derivatives, we take $(1 - \varphi)$ to be constant at $(1 - \varphi_{ss})$, because its value barely changes for small perturbations. This linear system has a solution of the form

$$\begin{pmatrix} \langle \mu \rangle \\ \langle \hat{\mu} \rangle \end{pmatrix} = \exp(st) \begin{pmatrix} B_1 \\ B_2 \end{pmatrix}, \quad (17)$$

where s represents the eigenvalue(s) of matrix A and (B_1, B_2) are the corresponding eigenvectors. Equation (17) is then substituted into (15), with differential terms in (15) expressed as $d\langle \mu \rangle/dt = B_1 s \cdot \exp(st)$ and $d\langle \hat{\mu} \rangle/dt = B_2 s \cdot \exp(st)$. This results in a quadratic equation in s :

$$s^2 - 2Cs + D^2 = 0, \quad (18)$$

where $C = (A_{11} + A_{22})/2$ and $D^2 = A_{11}A_{22} - A_{12}A_{21}$. This equation has the solution $s = C \pm \sqrt{C^2 - D^2}$. Therefore, the characteristics of the solution to equation set (14) are mostly described by the eigenvalues s that is by the signs of C and $C^2 - D^2$, while the eigenvector (B_1, B_2) determines the magnitudes and phase lags of shear stress and state. We discuss these two aspects in the following.

4.1. Frictional Stability Criterion

From the quadratic equation (18), we have instability when $\text{Re}(s) > 0$, where “Re” denotes the real part of a quantity. $\text{Re}(s) = 0$ gives the stability boundary corresponding to a critical stiffness, K_c . According to the solution to (18), this stability boundary is met when $C = 0$ and $D^2 > 0$. Substituting the A matrix ((16a)–(16d)), we know that D^2 is always positive. Evaluating $C = 0$ gives the critical stiffness

$$K_c = \frac{6H(1 - \varphi_{ss})\sigma_n}{L_t \lambda} \left[\frac{\hat{\mu}_{ss} (1 + \tilde{\mu}_{ss}^2)}{3 (1 - \tilde{\mu}_{ss} \hat{\mu}_{ss})^2} - \alpha_{\mu} \frac{(1 + \hat{\mu}_{ss}^2)}{(1 - \tilde{\mu}_{ss} \hat{\mu}_{ss})^2} \right]. \quad (19)$$

Meanwhile, at the neutral stability condition ($C = 0$), s is given by $s = \sqrt{C^2 - D^2} = \sqrt{-D^2} = \pm mi$ (here $m = |D|$ is termed angular frequency). Substituting expressions for D gives

$$m = \frac{6H(1 - \varphi_{ss})V_{\text{imp}}}{L_t \lambda} \sqrt{\frac{\hat{\mu}_{ss} (1 + \tilde{\mu}_{ss}^2)}{3\alpha_{\mu} (1 + \hat{\mu}_{ss}^2)} - 1}. \quad (20)$$

Recalling the steady state solution (10a)–(10c), the characteristic recurrence wavelength W_c of the associated persistent sinusoidal waves is

$$W_c = \frac{2\pi}{m} V_{\text{imp}} = \frac{\pi L_t \lambda}{3H(1 - \varphi_{ss}) \sqrt{\frac{\hat{\mu}_{ss} (1 + \tilde{\mu}_{ss}^2)}{3\alpha_{\mu} (1 + \hat{\mu}_{ss}^2)} - 1}}. \quad (21)$$

In summary, at $K = K_c$, a perturbation to the spring-block fault system will induce stable oscillations. When $C^2 > D^2$ and $C > 0$, perturbations grow monotonically. If $C^2 < D^2$ and $C > 0$, then oscillations occur with growing amplitude. If $C^2 > D^2$ and $C < 0$, then the perturbation decays exponentially. If $C^2 < D^2$ and $C < 0$, then oscillations occur with decaying amplitude.

4.2. Oscillation Magnitudes and Phase Lags

From (17), the general solution at neutral stability condition can be expressed in the form $\begin{pmatrix} \langle \mu \rangle \\ \langle \hat{\mu} \rangle \end{pmatrix} = \exp(mi)$

$\begin{pmatrix} B_1 \\ B_2 \end{pmatrix}$. Substituting this into (15) yields $(A - mi \cdot I) \begin{pmatrix} B_1 \\ B_2 \end{pmatrix} = 0$, where I is the identity matrix. This gives $B_2 = \frac{mi - A_{11}}{A_{12}} B_1$. By taking $B_1 = 1$, the general solution can be rewritten as

$$\begin{pmatrix} \langle \mu \rangle \\ \langle \hat{\mu} \rangle \end{pmatrix} = K_1 \begin{pmatrix} \cos mt \\ \frac{A_{11} \cos mt + m \sin mt}{A_{12}} \end{pmatrix} + K_2 \begin{pmatrix} \sin mt \\ \frac{m \cos mt - A_{11} \sin mt}{A_{12}} \end{pmatrix}, \quad (22)$$

where K_1 and K_2 are arbitrary constants. We go on to derive the particular solution for a given initial condition $(\langle \mu \rangle_0, \langle \hat{\mu} \rangle_0)$. Taking $t = 0$ defines the initial condition in equation (22), which gives the expressions for K_1 and K_2 , which are $K_1 = \langle \mu \rangle_0$ and $K_2 = \frac{A_{11} \langle \mu \rangle_0 + A_{12} \langle \hat{\mu} \rangle_0}{m}$. Therefore, the particular solution corresponding to the initial values $(\langle \mu \rangle_0, \langle \hat{\mu} \rangle_0)$ is expressed as

$$\begin{pmatrix} \langle \mu \rangle \\ \langle \hat{\mu} \rangle \end{pmatrix} = \langle \mu \rangle_0 \langle \hat{\mu} \rangle_0 \cos mt + \begin{pmatrix} \frac{A_{11} \langle \mu \rangle_0 + A_{12} \langle \hat{\mu} \rangle_0}{m} \\ \frac{A_{21} \langle \mu \rangle_0 + A_{22} \langle \hat{\mu} \rangle_0}{m} \end{pmatrix} \sin mt. \quad (23a)$$

Here we define $\langle \mu \rangle_{\text{half}}$ and $\langle \hat{\mu} \rangle_{\text{half}}$ as half the amplitudes of the shear stress and state oscillations, respectively, and $\Delta\Phi_\tau$ and $\Delta\Phi_\psi$ to be the corresponding phase lags relative to the imposition of the perturbation. With these definitions, the general solution (23a) is written as

$$\begin{pmatrix} \langle \mu \rangle \\ \langle \hat{\mu} \rangle \end{pmatrix} = \begin{pmatrix} \langle \mu \rangle_{\text{half}} \cos(mt - \Delta\Phi_\tau) \\ \langle \hat{\mu} \rangle_{\text{half}} \cos(mt - \Delta\Phi_\psi) \end{pmatrix}. \quad (23b)$$

Combining the above two equations ((23a) and (23b)) yields

$$\Delta\Phi_\tau = \tan^{-1} \left(\frac{A_{11} \langle \mu \rangle_0 + A_{12} \langle \hat{\mu} \rangle_0}{m \langle \mu \rangle_0} \right) \text{ and } \Delta\Phi_\psi = \tan^{-1} \left(\frac{A_{21} \langle \mu \rangle_0 + A_{22} \langle \hat{\mu} \rangle_0}{m \langle \hat{\mu} \rangle_0} \right), \quad (24a)$$

$$\langle \mu \rangle_{\text{half}} = \Delta\mu_{ss} \sec(\Delta\Phi_\tau) \text{ and } \langle \hat{\mu} \rangle_{\text{half}} = \Delta\hat{\mu}_{ss} \sec(\Delta\Phi_\psi). \quad (24b)$$

Let us consider a small velocity step from stable sliding at velocity V^0 to a new velocity V^1 . The initial condition can be determined as

$$\begin{pmatrix} \langle \mu \rangle_0 \\ \langle \hat{\mu} \rangle_0 \end{pmatrix} = \begin{pmatrix} -\Delta\mu_{ss} \\ -\Delta\hat{\mu}_{ss} \end{pmatrix}. \quad (25)$$

The negative signs indicate that the initial condition is evaluated at the prestep stable sliding state relative to the poststep steady state. Recalling the definitions that $\hat{\mu} \equiv \tan\psi$ and defining $b_\psi \equiv \partial(\hat{\mu}) / \partial(\ln V)$, we have $\langle \hat{\mu} \rangle_0 = b_\psi \ln(V^1/V^0)$. From the rate dependence of steady state friction, we have $\langle \mu \rangle_0 = (b - a) \ln(V^1/V^0)$. Therefore, $\langle \mu \rangle_0$ and $\langle \hat{\mu} \rangle_0$ are linearly related to each other, giving $\langle \mu \rangle_0 / \langle \hat{\mu} \rangle_0 = (b - a) / b_\psi$. Substituting this relation and the matrix A into (24a) and (24b) yields

$$\Delta\Phi_\tau = \tan^{-1} \left(\sqrt{\frac{a}{b-a}} \right) \text{ and } \Delta\Phi_\psi \approx 0, \quad (26a)$$

$$\langle \mu \rangle_{\text{half}} = \Delta\mu_{ss} \sqrt{\frac{b}{b-a}} \text{ and } \langle \hat{\mu} \rangle_{\text{half}} = \Delta\hat{\mu}_{ss}. \quad (26b)$$

Accordingly, the amplitudes of shear stress and state (porosity) oscillations can be calculated as

$$\Delta\mu_s = 2|\langle \mu \rangle_{\text{half}}| = 2\sqrt{b(b-a)} \left| \ln \left(\frac{V^1}{V^0} \right) \right|, \quad (27)$$

$$\Delta\varphi_s = 2|\Delta\varphi_{ss}|$$

The subscript “s” indicates that the stress drop derived here is from a (quasi)static analysis, which is distinguished from the dynamic stress drop that emerges when inertia starts to play a role (Rice & Tse, 1986). Note that the above analysis only gives the oscillatory solution at the neutral stability boundary ($K = K_c$). Near the condition of neutral stability, the amplitudes of the oscillations are expected to grow or die (attenuate) depending on the sign of $C^2 - D^2$. The wavelength of the growing (or attenuating) oscillations is supposed to be of the same order as W_c .

4.3. Equivalent RSF Parameters and Consistency With Rice and Ruina’s Theory

In Paper 1, by analytically solving the constitutive equations of the CNS model, we have obtained physically meaningful, analytical expressions for the classical RSF parameters, a , b and D_c :

$$\begin{aligned} a &\equiv \frac{\partial \tilde{\mu}}{\partial(\ln V)} \frac{\partial \mu}{\partial \tilde{\mu}} \Big|_{\psi=\psi_{ss}} = a_\mu \frac{(1 + \hat{\mu}_{ss}^2)}{(1 - \tilde{\mu}_{ss} \hat{\mu}_{ss})^2}, \\ b &\equiv \frac{\partial \hat{\mu}}{\partial(\ln V)} \frac{\partial \mu}{\partial \hat{\mu}} \Big|_{V=V_{ss}} = b_\psi \frac{(1 + \tilde{\mu}_{ss}^2)}{(1 - \tilde{\mu}_{ss} \hat{\mu}_{ss})^2}, \\ D_c &\equiv -\frac{V \partial \varphi}{\partial(d\varphi/dt)} = \frac{L_t \lambda}{2HN(M + N)(1 - \varphi_{ss})}. \end{aligned} \quad (28)$$

The friction rate-dependent parameters a and b are expressed in the conjugated form, where a_{\sim} and b_{ψ} are the logarithmic rate dependences of the grain boundary friction $\tilde{\mu}$ and the dilatant friction $\hat{\mu}$, respectively. The critical slip distance, D_c , is derived from the state evolution of a shearing gouge (porosity in our case) in response to a small perturbation. It is apparent from the expression that D_c is indeed a characteristic length scale that is proportional to the shear band thickness ($L_t \lambda$) and related to the microstructural (constant) parameters of the gouge (H , M , and N values).

A general form of critical stiffness for a single-degree-of-freedom system, not restricted to RSF laws, has been given by Rice and Ruina (1983):

$$K_c = -\frac{V}{D_c} \frac{d\tau_{ss}(V)}{dV}. \quad (29)$$

Here $\tau_{ss}(V)$ is the steady state shear stress at sliding velocity V . Using the rate-dependent shear strength $d\tau_{ss}(V)/d(\ln V) = \sigma_n(a - b)$, this expression can be expressed as a function of RSF parameters as $K_c = \sigma_n(b - a)/D_c$. As stated before, the CNS model can also be taken as a single state-variable system, so that the critical stiffness offered by Rice and Ruina (1983) also applies to the CNS model. Substituting the expressions for a , b , and D_c given in Paper 1 (equation (28)), and $b_{\psi} = \hat{\mu}_{ss}/(M + N)$, and $M = 2$, $N = 1$ for diffusion-controlled pressure solution, the general expression for K_c (equation (29)) can be written as

$$K_c = \frac{6H(1 - \phi_{ss})\sigma_n}{L_t \lambda} \left[\frac{\hat{\mu}_{ss}}{3} \frac{(1 + \tilde{\mu}_{ss}^2)}{(1 - \tilde{\mu}_{ss}\hat{\mu}_{ss})^2} - a_{\sim} \frac{(1 + \hat{\mu}_{ss}^2)}{(1 - \tilde{\mu}_{ss}\hat{\mu}_{ss})^2} \right]. \quad (30)$$

This expression is identical to the one obtained from our linearized stability analysis (cf. equation (19)).

A general expression for critical recurrence wavelength has also been given (Rice & Ruina, 1983; Ruina, 1983):

$$W_c = 2\pi D_c \sqrt{\frac{a}{b - a}}. \quad (31)$$

Similarly, substituting the RSF parameters derived into (31) yields the same expression for W_c as the one obtained from our stability analysis (cf. equation (21)).

What is new here compared to Rice and Ruina's work is that our stability analysis also yields an expression for the static stress drop, as given in (27), which scales with the logarithm of the size of the velocity perturbation and a mixed frictional parameter $\sqrt{b(b - a)}$. Substituting the equivalent RSF parameters yields

$$\begin{aligned} \Delta\mu_s &= 2\sqrt{b(b - a)} \left| \ln\left(\frac{V^1}{V^0}\right) \right| \\ &= 2\sqrt{b_{\psi} \frac{(1 + \tilde{\mu}_{ss}^2)}{(1 - \tilde{\mu}_{ss}\hat{\mu}_{ss})^2} \left[b_{\psi} \frac{(1 + \tilde{\mu}_{ss}^2)}{(1 - \tilde{\mu}_{ss}\hat{\mu}_{ss})^2} - a_{\sim} \frac{(1 + \hat{\mu}_{ss}^2)}{(1 - \tilde{\mu}_{ss}\hat{\mu}_{ss})^2} \right]} \left| \ln\left(\frac{V^1}{V^0}\right) \right|. \end{aligned} \quad (32)$$

A similar relation has not been reported for the classical RSF laws.

5. Unstable Slip Regime Predicted by the CNS Model ($V_{s \rightarrow w}$ and $V_{w \rightarrow s}$)

Different regimes of deformation from slow to high slip rates are captured by our model. Unstable slip potentially occurs only in the velocity-weakening regime, which, as shown in Figure 2, is bounded by two characteristic slip rates, $V_{s \rightarrow w}$ and $V_{w \rightarrow s}$. Both velocities are considered to be geologically meaningful: $V_{s \rightarrow w}$ is the velocity indicating the transition from flow to friction, and $V_{w \rightarrow s}$ is referred to as the minimum steady state stress velocity characterizing a velocity-weakening material (e.g., Hawthorne & Rubin, 2013), which as revealed by recent studies, can offer a compelling explanation for the aseismic slip behavior observed in subduction zones (note $V_{w \rightarrow s}$ is slightly different from the cutoff velocity usually introduced by the extended RSF laws to make the transition (Shibazaki & Shimamoto, 2007)). In order to constrain the unstable slip regime, in the following, we will derive the analytical expressions for these two velocities.

5.1. Transition From Velocity Weakening to Strengthening: $V_{w \rightarrow s}$

At a certain cutoff velocity, the profile of steady state friction coefficient versus slip rate reaches a minimum, yielding zero ($a - b$). Using the analytical expressions derived for a and b (equation (28)), one could have

$$\frac{\tilde{a}_\mu}{(1 + \tilde{\mu}_{ss}^2)} = \frac{b_\psi}{(1 + \hat{\mu}_{ss}^2)}. \quad (33a)$$

As given in Paper 1, the steady state solution for a general creep law such as equation (4a) gives

$$\hat{\mu}_{ss} \equiv \tan \psi_{ss} = H \left[\frac{L_t \lambda}{H V_{imp}} E_{pl}(T, d, \sigma_n) \right]^{\frac{1}{(M+N)}}. \quad (33b)$$

By definition, we have $b_\psi = (\hat{\mu}_{ss}) / (\ln V) = \hat{\mu}_{ss} / (M + N)$. Meanwhile, the grain boundary friction coefficient is expressed as

$$\tilde{\mu} = \tilde{\mu}^* + \tilde{a}_\mu \ln(V_{imp}/V^*). \quad (33c)$$

Combining equations (33a)–(33c), one can solve the transition velocity $V_{w \rightarrow s}$ numerically.

In the frictional regime, especially at high slip rates, the inequality $(\hat{\mu}_{ss})^2 \ll (\tilde{\mu}_{ss})^2 < 1$ holds firmly, such that equation (33a) can be reformulated as

$$\frac{\tilde{a}_\mu}{(1 + \tilde{\mu}_{ss}^2)} = \frac{\hat{\mu}_{ss}}{(M + N)}. \quad (34)$$

Given a typical \tilde{a}_μ value of 0.006 and $\tilde{\mu}^*$ of 0.6, the value of the term $(1 + \tilde{\mu}_{ss}^2)$ barely changes (i.e., changes from 1.36 to 1.43 as velocity increases by 10 orders of magnitude) and can thus be taken as a constant with a value of $(1 + \tilde{\mu}^{*2})$. Substituting (33b) into (34) and solving the equation gives

$$V_{w \rightarrow s} \approx \frac{L_t \lambda E_{pl}(T, d, \sigma_n)}{H} \left[\frac{H(1 + \tilde{\mu}^{*2})}{\tilde{a}_\mu (M + N)} \right]^{(M+N)}. \quad (35a)$$

This relation indicates that $V_{w \rightarrow s}$ is proportional to the slip zone thickness ($L_t \lambda$) and the compactional creep rate as governed by the creep law (E_{pl}). For the latter, other parameters such as temperature T , grain size d , and effective normal stress σ_n play their roles. This transition velocity is also influenced by the microstructural and material properties (H , M , and N values).

The steady state solution suggests a scaling relation such that $\hat{\mu} \propto V^{-1/(M+N)}$ (see equation (33b) for a general creep law and (10b) for a linear law of pressure solution). With respect to a reference velocity V^* , equation (35a) can thus be reformulated as

$$V_{w \rightarrow s} \approx V^* \left[\frac{\hat{\mu}^* (1 + \tilde{\mu}^{*2})}{\tilde{a}_\mu (M + N)} \right]^{(M+N)}. \quad (35b)$$

Here $\hat{\mu}^*$ is the dilatant friction at V^* . Adopting the equivalent expressions for a and b ((28)), the above equation can be rewritten as

$$V_{w \rightarrow s} \approx V^* (b/a)^{(M+N)}. \quad (35c)$$

This relation is insightful for estimating a transition velocity from experiments. Note that the a and b values are the specific quantities (measured) at V^* , and the cutoff velocity obtained from (35c) only applies to the simulated fault under the experimental conditions. For extrapolation to natural faults, the result obtained from (35c) needs to be rescaled on basis of the in situ fault conditions ($L_t \lambda$, T , d , and σ_n).

5.2. Transition From Flow to Friction: $V_{s \rightarrow w}$

Like the transition at the cutoff velocity, the transition from flow to friction can be specified as $d\mu_{ss}/d(\ln V) = 0$. As a first-order approximation, this relation is satisfied when the two end-member shear accommodat- ing processes (namely, granular flow and ductile/plastic shear creep) share the same strength, and the

transition velocity $V_{s \rightarrow w}$ can be obtained if we let the two analytical solutions be equal (see Figure 2 and equations (13) and (16) in Paper 1). However, to predict $V_{s \rightarrow w}$ in this way is perhaps unwarranted because of the following reasons. First, as given by equation (3a), the shear creep is attributed to both the shear band ($L_t \lambda_{pl}^{sb}$) and the bulk layer ($L_t (1 - \lambda)_{pl}^{bulk}$), both of which have distinct thickness, grain sizes, and porosities. Second, multiple microscopic processes might accommodate the shear creep. Finally, the geometrical constant for describing the (tangential) shear creep (A_t value in (38)) would be different from that for the normal creep (A_n value in (8a)), not to mention that the A_t values might be different between the shear band and bulk layers. Some of these tricky points are explained later in our numerical implementation (section 6).

Here we propose an alternative approach to estimate $V_{s \rightarrow w}$. As slip rate decreases, the average dilatancy angle will increase and the porosity will decrease. As porosity approaches a (near) zero, terminal porosity (φ_0), dilatant granular flow will be inhibited or at least contribute negligibly to the strength (Figure 2). Accordingly, sample shear deformation is accommodated by shear creep at grain contacts, rendering the fault system into a flow regime. Therefore, the transition between friction and flow is to the first order limited by the terminal porosity φ_0 . According to the definition that $\hat{\mu} \equiv \tan \psi = H(q - 2\varphi)^N$, the dilatant frictional strength reaches the maximum at φ_0 , that is,

$$\hat{\mu}_{\max} = H(q - 2\varphi_0)^N. \quad (36a)$$

From this, we can further estimate the maximum frictional strength:

$$\mu_{\max} \approx \frac{\tilde{\mu}^* + \hat{\mu}_{\max}}{1 - \tilde{\mu}^* \hat{\mu}_{\max}}. \quad (36b)$$

Based on ((36a)) and ((36b)), the transition velocity from flow to friction can be determined as

$$V_{s \rightarrow w} \approx \frac{L_t \lambda E_{pl}(T, d, \sigma_n)}{H(q - 2\varphi_0)^{N(M+N)}}. \quad (37a)$$

Relative to a reference velocity V^* , which corresponds to a steady state porosity φ^* , (37a) can be reformulated as

$$V_{s \rightarrow w} = V^* \left(\frac{\varphi_c - \varphi^*}{\varphi_c - \varphi_0} \right)^{N(M+N)}. \quad (37b)$$

Similar to (35c), this equation provides a means to estimate the flow-to-friction transition velocity from laboratory experiments or alternatively to estimate the values of the exponents for the given conditions.

6. Numerical Implementation and Validation of the Analytical Results

To verify the theoretical analyses above, we perform numerical experiments and compare the results with the analytical solutions. The model geometry and the pressure-temperature conditions are the same as those previously used by Chen and Spiers (2016), which mainly involves (1) a 50 μm thick shear band localized at the margin of a 0.8 mm thick calcite gouge layer; (2) average grain sizes of 2 μm and 20 μm in the shear band and bulk gouge, respectively; and (3) under 50 MPa effective normal stress and 80°C hydrothermal conditions. We simulate the frictional behavior of this simulated gouge after some displacement where the gouge has reached a more or less steady state microstructure as described above. Under these conditions, intergranular flow and diffusion-controlled IPS have been inferred to be the dominant deformation mechanisms (Chen et al., 2015a). The compactional creep can be described by a linear law as (8a), and we assume the same mechanism for the shear creep, which can be written as

$$\dot{\gamma}_{pl}^{sb} = \frac{A_t(DCS)\Omega}{RTd^3} \frac{\tau}{(q - 2\varphi)^2}. \quad (38)$$

The parameters in (38) are the same as in (8a) except that A_t is a geometrical constant for tangential creep. Note that equation (38) applies to the shear band and a similar one can be written for the bulk layer but with different grain size and (critical) porosity. We assume the same A_t value for both layers.

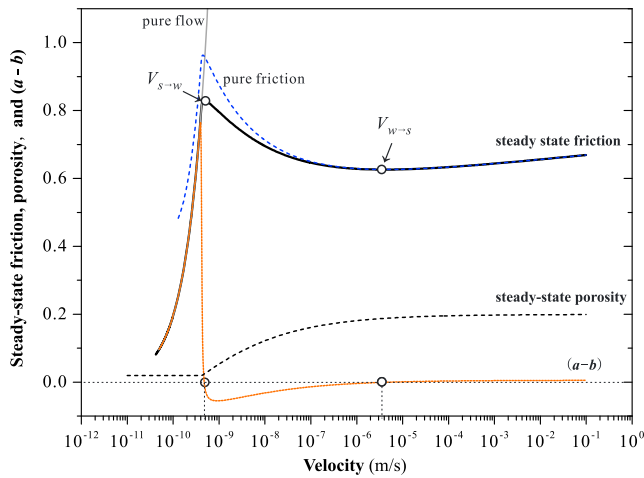


Figure 3. The model prediction of steady state friction coefficient, porosity, and $(a - b)$ as a function of the logarithm of load point velocity, for a simulated carbonate fault sheared at hydrothermal conditions. The analytical results for the two end-member cases (pure friction and pure flow controlled deformation) are added for comparison. All the features are generally the same as in Figure 2. See detailed explanation in the text.

As in our previous study (Chen & Spiers, 2016) and Paper 1, the ODEs of equations (4a)–(4c), with (5a), (5b), (8a)–(8c), and (38), are solved using the finite element package COMSOL. For a detailed explanation and values of the parameters, see Chen and Spiers (2016) and also Paper 1.

6.1. Steady State Shear Strength Profile and Unstable Slip Regime ($V_{s \rightarrow w}$ and $V_{w \rightarrow s}$)

We first simulate the steady state by setting $\dot{\tau}$ and $\dot{\phi}$ in equations (4a) and (4b) to be zero. Figure 3 presents the steady state friction coefficient and its rate dependence $(a - b)$, as well as the steady state porosity, with slip rates spanning from ~ 0.1 nm/s to 0.1 m/s. The friction profile predicted shows consecutive transitions between stable and potentially unstable slip regimes and the corresponding $(a - b)$ values change from positive to negative and back to positive with increasing slip rate. The steady state porosity is constant at a near-zero level in the flow regime, while in the frictional regime it increases as slip rate increases, asymptotically reaching ϕ_c at high slip rates. All these features are generally the same as the prediction for a general creep law (cf. Figure 2). Here we have two more notes for the flow regime.

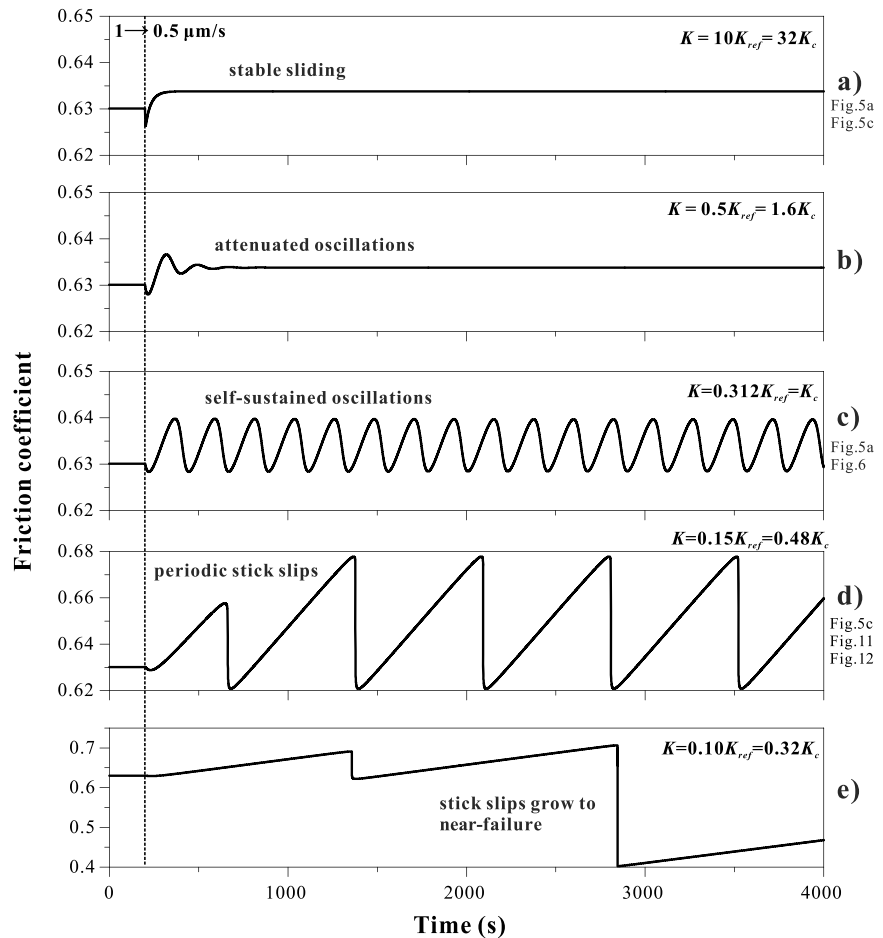


Figure 4. (a–e) Numerical modeling results of the CNS model, showing friction coefficient versus shear time. The load point speed is suddenly changed from steady sliding at 1 $\mu\text{m/s}$ to 0.5 $\mu\text{m/s}$. Subsequent fault motions for various apparatus stiffness are modeled. In Figure 4e, the required numerical accuracy was not sufficient to resolve the large stick slips.

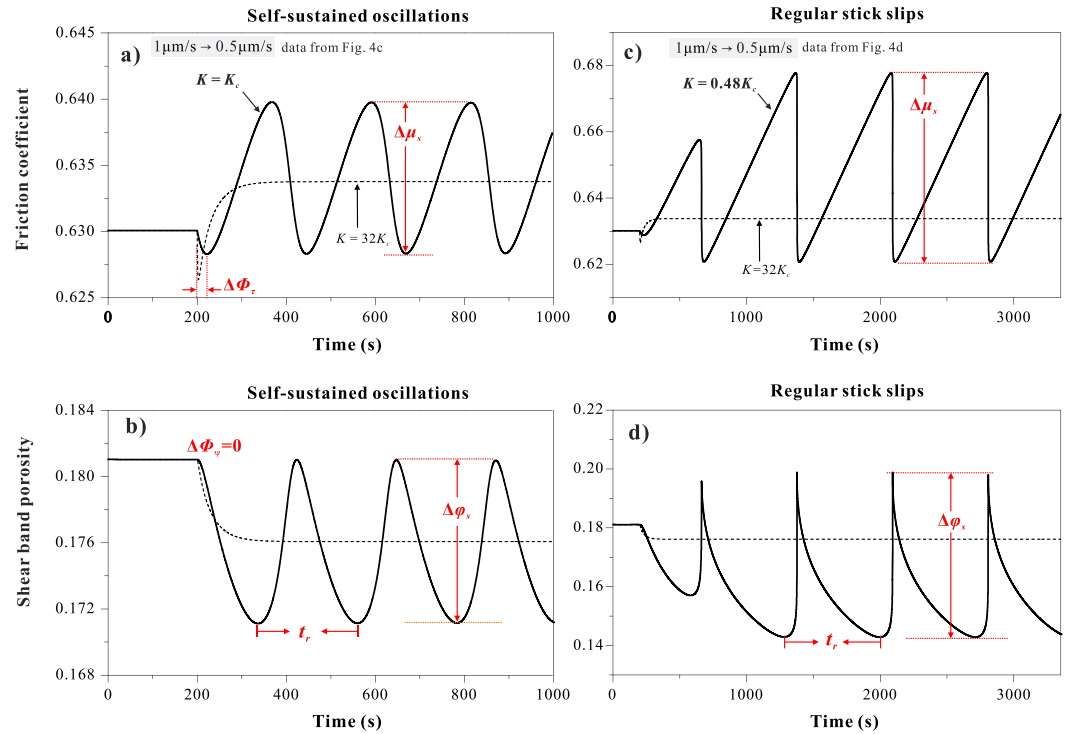


Figure 5. Modeling results showing details of the evolution of friction coefficient and state in self-sustained oscillations and regular stick slips, also shown in Figures 4b and 4c. Results simulated at high stiffness are added for comparison (gray dashed lines). Definitions of the parameters indicated in the figure ($\Delta\mu_s$, $\Delta\phi_s$, $\Delta\phi_v$, $\Delta\phi_{pl}$ and t_r) are explained in detail in the text.

First, the flow strength predicted at very low slip rates shows a strong velocity dependence. We infer this to be due to the linear creep law adopted for pressure solution. For a general creep law of a power law form $\dot{\gamma} \propto \tau^n$, where n is the stress exponent, it is easy to show that $(a - b) = a = \mu_{ss}/n$ in the flow regime. As a special case, $n = 1$ causes $(a - b)$ to be equal to μ_{ss} (Figure 3). For dislocation creep, n is expected to take values of 3.5–11 (De Bresser et al., 2002) and $(a - b)$ would thus be much lower but still positive.

Second, a steady state flow stress is only achieved when a gouge compacts to a near zero, threshold porosity (e.g., Niemeijer et al., 2002). In order to incorporate this terminal porosity ϕ_0 , we make a slight modification to the porosity function, but only apply it to the compaction part (cf. equations (8a)–(8c)):

$$f_{pl}(\phi) = (q - 2\phi)^{-2} \left(\frac{\phi - \phi_0}{\phi_c - \phi_0} \right). \quad (39)$$

This function causes a gouge to compact asymptotically to ϕ_0 in the flow regime, at which point the compaction creep rate becomes zero and a steady state is attained, while in the frictional regime where the gouge has higher porosities, it exhibits similar behavior to equation (8b). In the results shown in Figure 3, we assume ϕ_0 to be 2%. As addressed earlier, the geometric constant A_t is poorly constrained and here it is assumed to be 2 times the A_n value. To investigate the sensitivity of the model prediction to these parameters, we have varied the ϕ_0 value from 0 to 5% and used different A_t values, that is, 0, $1A_n$, and $5A_n$. As given in Figure S1 in the supporting information, the steady state profile is not affected by the A_t or ϕ_0 value for the frictional regime, and only the flow-to-friction transition is sensitive to these parameters. The larger these values, the higher the transition velocity $V_{s \rightarrow w}$ will be. A higher ϕ_0 value also causes the maximum frictional strength to be lower, as determined by equations (36a) and (36b). It is apparent from these exercises that it is difficult to determine $V_{s \rightarrow w}$ by equalling the shear strength of pure creep and pure friction, basically because of the poor constraints on the flow parameters (Figure S1).

Fortunately, the steady state porosity curve predicted by the model shows that the flow-to-friction transition occurs at the velocity where the porosity reaches the minimum (Figure 3), supporting our theoretical analysis

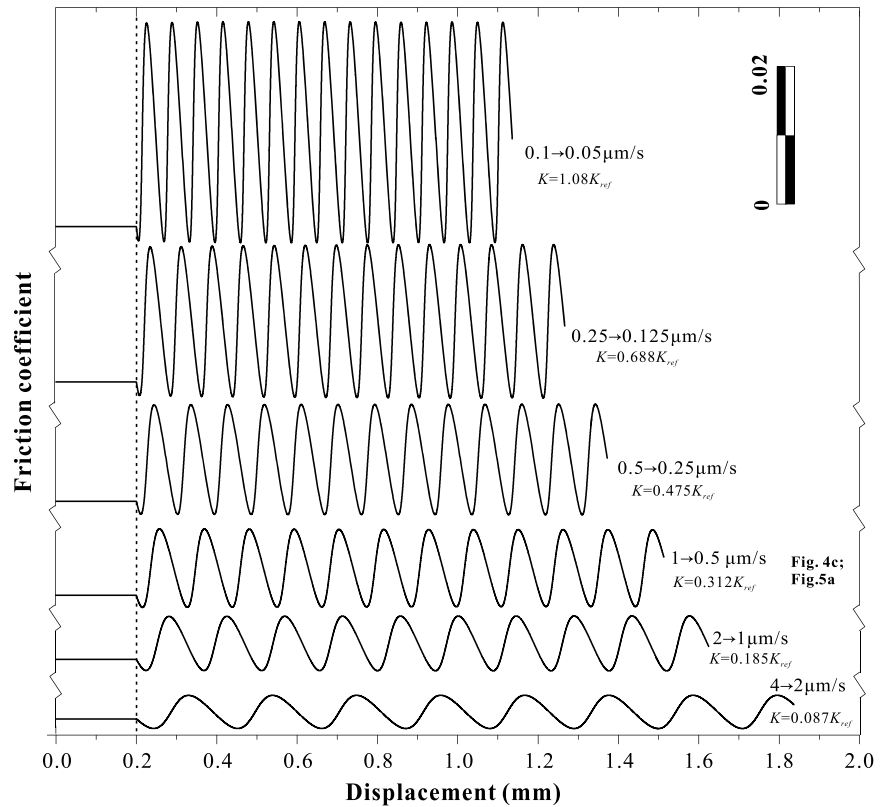


Figure 6. A series of simulations showing self-sustained oscillations at variable sliding velocities. All the simulations investigate 0.5-fold velocity steps. In each case, we vary the stiffness until self-sustained oscillations appear.

in section 5.2. For a calcite gouge at the simulated conditions (50 MPa and 80°C hydrothermal conditions), the transition velocity $V_{s \rightarrow w}$ calculated from (37b) is ~ 1 nm/s. The maximum frictional strength μ_{\max} calculated from (36b) is ~ 0.82 , and its value increases with decreasing ϕ_0 value. All these results are consistent with the numerical results (Figures 3 and S1). As for the transition velocity $V_{w \rightarrow s}$, equation (35a) predicts a value of $4.5 \mu\text{m/s}$, which is fully consistent with the numerical result (Figure 3) and also with previous experiments performed at similar conditions (Chen et al., 2015a). Moreover, using the a and b values obtained by performing numerical velocity stepping tests at different slip rates ($0.1 \mu\text{m/s}$ to $100 \mu\text{m/s}$), the $V_{w \rightarrow s}$ values calculated from (35c) fall between 4.3 and $4.8 \mu\text{m/s}$, again in favorable agreement with the numerical result (Figure 3). All these calculations support our proposed idea to determine $V_{w \rightarrow s}$ and $V_{s \rightarrow w}$ from laboratory experiments, using equation (35c) and (37b), respectively. These equations are concise, and more importantly, without concerning the individual flow parameters (e.g., A_t) are easily applicable in practice.

6.2. Transient Behavior and Validation of the Slip Stability Criterion

The steady state analysis above predicts the unstable slip regime, that is, bounded by $V_{s \rightarrow w}$ and $V_{w \rightarrow s}$. To verify our linear stability analysis results, the following three series of simulations are conducted in this regime, investigating the effects of spring stiffness, slip rate, and perturbation size, respectively.

6.2.1. Variable Spring Stiffness and the Full Spectrum of Fault Slip Behavior

First, numerical modeling was performed under a wide range of stiffness values, investigating a velocity step from 1 to $0.5 \mu\text{m/s}$, which represents a small perturbation to the simulated fault system. Representative results for the evolution of the friction coefficient are given in Figure 4. Generally, with decreasing stiffness, the fault system shows a transition from stable to unstable sliding behavior. All models start with an instantaneous or gradual change in frictional strength upon the change in load point velocity, which is followed by an exponential decay to a new steady state (Figure 4a), or by oscillations which attenuate to a steady state

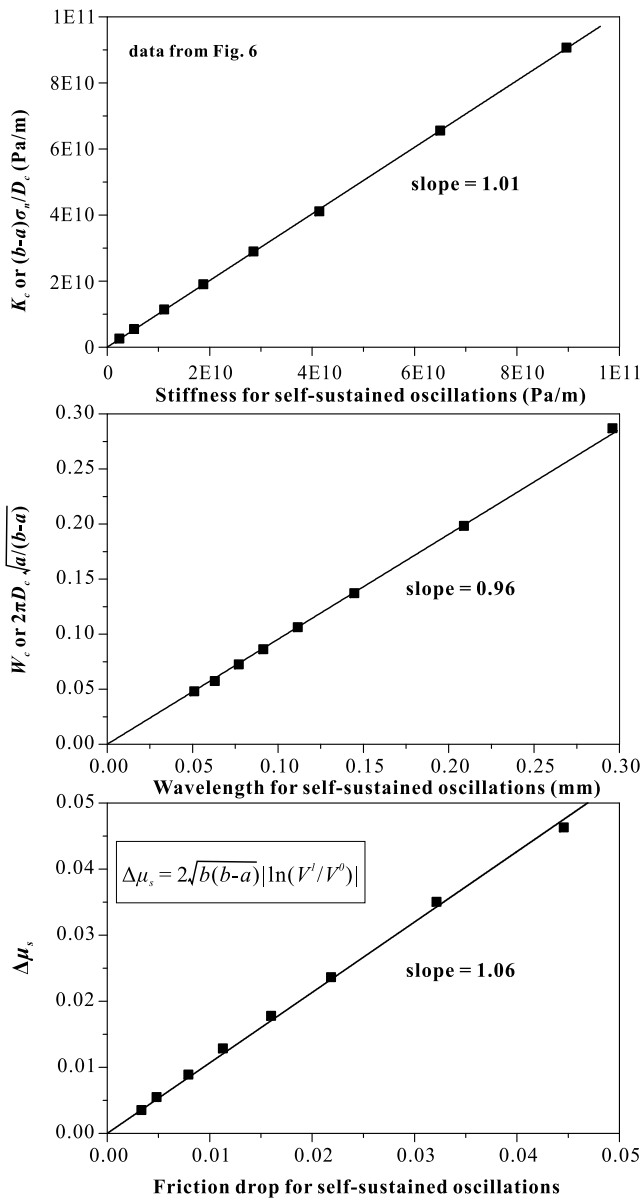


Figure 7. Comparison of (a) the critical stiffness K_c , (b) the recurrence wavelength W_c , and (c) the amplitude of the oscillations (or stick slips) between the values obtained from the linearized stability analysis and those from the numerical modeling results (Figure 6). In the simulations, we varied the fault stiffness until self-sustained oscillations or regular stick slips occur.

either constants (σ_n , H , L_t^2 , and α_μ^-) or some steady state variables (ϕ_{ss} , $\tilde{\mu}_{ss}$, and $\hat{\mu}_{ss}$). The latter can be determined from the steady state solution given in Paper 1. In Figure 7, the values of K_c , W_c , and $\Delta\mu_s$ predicted by the analytical expressions are plotted against those measured in the numerical simulations. As expected, the two sets of data correlate well with one another, for all three quantities, as indicated by the regression slopes of about 1.

6.2.3. Variable Perturbation Size Series and the Static Stress Drop ($\Delta\mu_s$)

Third, we performed simulations with velocity steps that have the same poststep velocity. In other words, we simulate perturbations of different sizes and senses (e.g., $0.47 \rightarrow 0.5 \mu\text{m/s}$ and $5.0 \rightarrow 0.5 \mu\text{m/s}$). Again, in each case, we varied the spring stiffness until SSO or RSS behavior appeared, which marks the neutrality of frictional stability. Figure 8 presents the results from the upward velocity steps. Clearly, as the perturbation

(Figure 4b) or which are sustained with the same amplitude (Figure 4c), or by regular stick slips (Figure 4b). For very low stiffness, these stick slips grew in size that could not be resolved numerically (Figure 4e).

In the present study, we focus on the slip stability of a fault system, for which two kinds of behavior predicted above are particularly interesting. One is a regime of self-sustained oscillations (SSO), which occurs in the “neutral stability” regime, where the spring stiffness (K) should be comparable to the critical stiffness of the gouge (K_c) (Gu & Wong, 1991; Tullis & Weeks, 1986; Weeks & Tullis, 1985). Another is the regular stick slips (RSS), characterized by periodic recurrence intervals and static stress drops, which are often observed in laboratory experiments and thought to be representative of earthquakes on natural faults (Byerlee, 1970; Scholz, 2002). Details of the simulation results that show the evolution of friction coefficient and state (porosity) of the gouge for the SSO and RSS behaviors are shown in Figures 5a–5d, respectively. To compare with the analytical expressions obtained in section 4, we measure three quantities in the simulation results: (1) the static stress drops and porosity changes ($\Delta\mu_s$ and $\Delta\phi_s$), which are measured as the difference between the peak and trough values from the periodic parts of the corresponding curves, respectively; (2) the recurrence time (or wavelength when plotted as a function of displacement) of the oscillations or stick slips (t_r or W_r); and (3) for the SSO behavior, the phase lags in friction coefficient and porosity ($\Delta\Phi_\tau$ and $\Delta\Phi_\psi$), defined as the phase shift relative to the time of the imposition of the perturbation. In the above simulations with different stiffness (Figure 4), SSO behavior occurs when the stiffness is equal to or slightly lower than the critical stiffness and it gradually evolves into RSS behavior as stiffness decreases (see more results in Figure S2). It is evident that as the stiffness decreases, the $\Delta\mu_s$ and $\Delta\phi_s$ values, and the t_r and W_r values all increase (Figure 4).

6.2.2. Variable Slip Rates Series and the Critical Stiffness K_c

Second, we performed simulations with velocity steps that have the same (small) size of perturbations (e.g., $0.1 \rightarrow 0.05$ and $4.0 \rightarrow 2.0 \mu\text{m/s}$). In each case, we varied the spring stiffness until SSO behavior appeared. As shown in Figure 6, the results of friction coefficients are plotted against the displacement of the slider (imposed displacement minus the spring stretch).

As the sliding velocity decreases, the results clearly show that (1) the stiffness needed to produce the SSO behavior (K_c) increases, (2) the recurrence wavelengths (W_c) slightly decrease, and (3) the amplitudes of the oscillations ($\Delta\mu_s$) increase. We next compare the measured quantities of K_c , W_c , and $\Delta\mu_s$ with those calculated from our theoretical analyses. Note that the parameters appearing in these expressions are

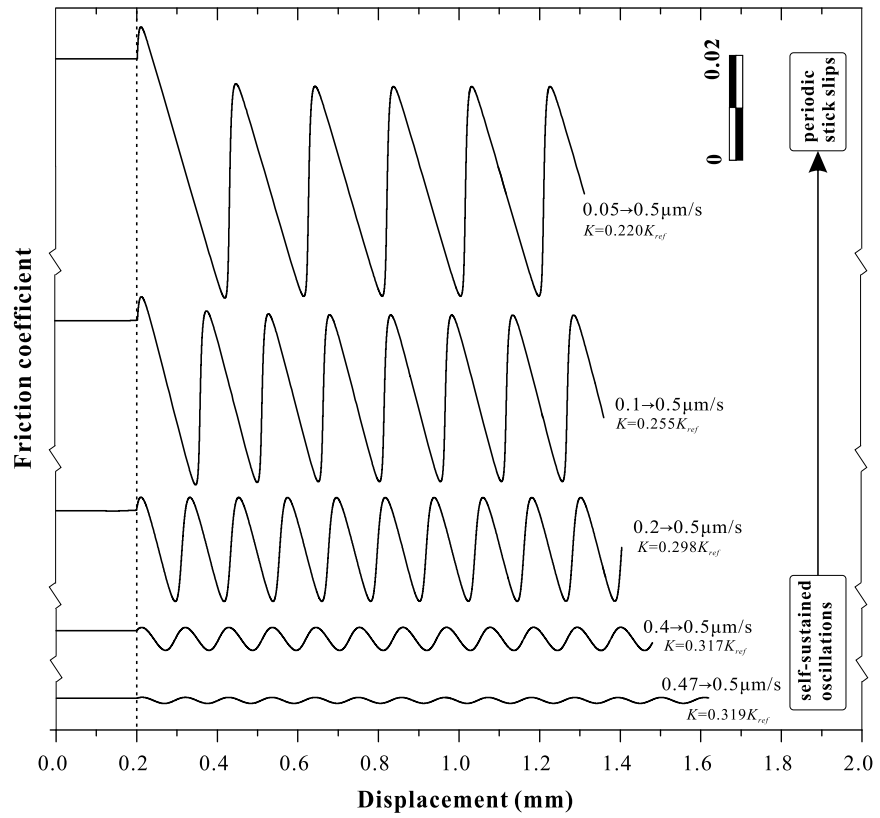


Figure 8. A series of simulations showing self-sustained oscillations (or stick slips) with variable magnitude of velocity steps. All the simulations involve steps to 0.5 μm/s. In each case, we vary the stiffness until self-sustained oscillations or regular stick slips appear.

size increases, a transition from SSO to RSS behavior occurs. Correspondingly, the static stress drops ($\Delta\mu_s$) and recurrence wavelengths (W_c) increase, whereas the stiffness to produce these behaviors again show an increasing trend but the values vary in a small range (0.220 – 0.319 K_{ref}), which corresponds to the changes in the critical stiffness with perturbation size. The highest stiffness (0.319 K_{ref}) is obtained from the case with the smallest size of perturbation (0.47 → 0.5 μm/s), with the value being identical to the one obtained from the linear stability analysis. The same trend applies to W_r , that is, the value determined from the smallest V step simulated (0.47 → 0.5 μm/s) is consistent with the critical value from the stability analysis. The amplitude of porosity change ($\Delta\phi_s$) and the phase lags for shear stress and porosity ($\Delta\Phi_\tau$ and $\Delta\Phi_\nu$) obtained from the numerical simulations are also consistent with the analytical predictions ($\Delta\Phi_\tau = \tan^{-1}(\sqrt{a/(b-a)})$, $\Delta\phi_s = 2\Delta\phi_{ss}$, and $\Delta\Phi_\nu = 0$, equations (26a), (26b), and (27)). For instance, for the V step of 1.0 → 0.5 μm/s, the porosity change and the $\Delta\Phi_\tau$ value associated with the SSO behavior are 0.97% and 0.89, respectively (see Figure 5), which are comparable to the results predicted by the analytical expressions, that is, $\Delta\phi_s$ of 0.99% and $\Delta\Phi_\tau$ of 0.77. The most consistent result occurs in the simulation with the smallest step (i.e., 4.7 → 5 μm/s), while for simulations with large perturbation size (where stick slips occur), the analytical solutions do not apply.

6.2.4. Summary of Unstable Slip Behavior

Combining now the results from all the three series of simulations presented above, we can further investigate the static stress drop and recurrence time (t_r) associated with the SSO and RSS behaviors, which can be taken as the “characteristic” earthquakes on a seismogenic fault (e.g., Schwartz & Coppersmith, 1984). The static stress drop $\Delta\mu_s$ is found to exhibit (1) a decrease with an increase in the logarithm of poststep velocity $\ln(V^1)$ (Figure 9a), (2) a linear relation with $\sqrt{b(b-a)}$ (Figure 9b), and (3) a log linear relation with the velocity perturbation size ($|\ln(V^1/V^0)|$) (Figure 9c). All these features observed in the numerical simulations are consistent with the analytical result for $\Delta\mu_s$ from the linearized stability analysis ($\Delta\mu_s = 2\sqrt{b(b-a)}|\ln(V^1/V^0)|$).

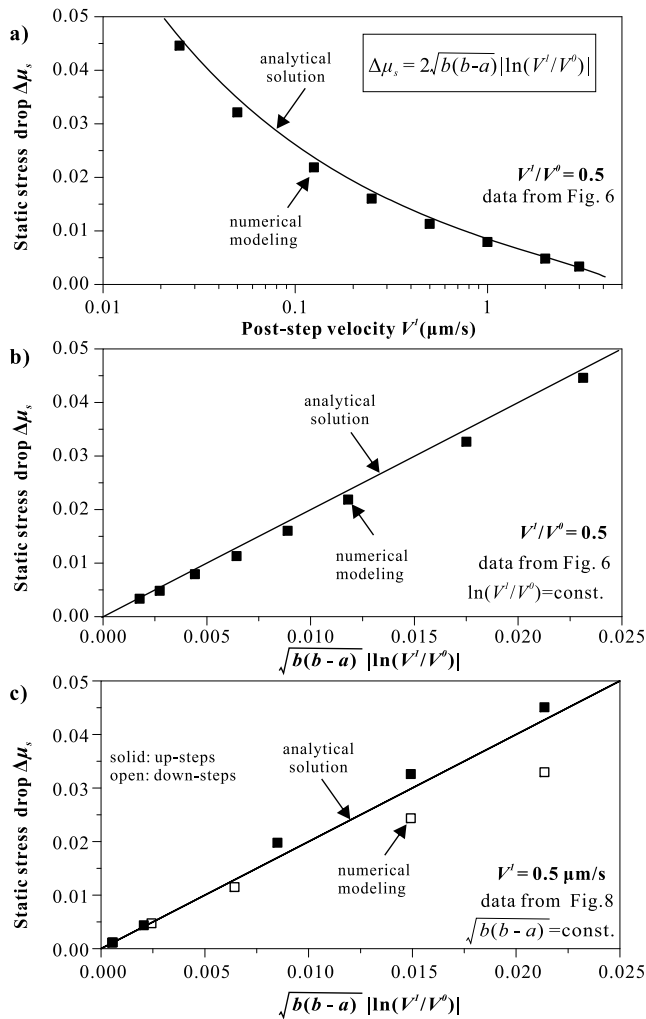


Figure 9. Dependence of static stress drop associated with self-sustained oscillations or stick slips ($\Delta\mu_s$) on varied parameters, (a) the poststep velocity V^1 , (b) the value of $(b(b-a))^{0.5}$, and (c) the magnitude of the velocity perturbation $|\ln(V^1/V^0)|$. All the results are obtained from the simulations shown in Figures 6 and 8.

Following previous work (e.g., Beeler et al., 2014; Karner & Marone, 2000), we plot the $\Delta\mu_s$ data against $\ln(t_r)$. As shown in Figure 10, the increase in $\Delta\mu_s$ with $\ln(t_r)$ seems to display two distinct trends. One is the change of $\Delta\mu_s$ over a wide range of sliding velocities and with a gentle slope, shown by data from the simulations that have the same step size but different velocities (Figure 6); the other indicates a steeper slope, demonstrated by data from simulations with variable perturbation size and stiffness (Figures 4, 8, and S2). The friction behavior in the second trend involves a transition from SSO to RSS behavior (the inset of Figure 10). In the case of SSO behavior, the relation of $\Delta\mu_s$ versus $\ln(t_r)$ obtained from the numerical simulations is consistent with the analytical prediction of critical recurrence time ($t_r = W_c/V_{\text{imp}}$). For the stick slips, the modeling results fit with the prediction for upward velocity steps. As the stiffness decreases further from the critical value, the results of $\Delta\mu_s$ versus t_r appear to follow a linear relation. We infer this is because most of the recurrence time is in the “stick” period, during which the shear stress accumulates more or less following the elastic loading curve that gives $\Delta\mu_s \approx Vt_rK/\sigma_n$.

6.3. Regular Stick-Slip Events Predicted by the CNS Model

In the unstable regime ($K < K_c$), regular stick slips are predicted by our model (Figure 4d, see more results in Figure S2). During a stick slip, the slip rate of the sample can be orders of magnitude higher than the imposed velocity. To gain insight into this, we compare the evolution of macroscopic friction coefficient (μ) and its two components, namely, grain boundary friction and friction due to intergranular dilatation ($\tilde{\mu}$ and $\hat{\mu}$), against time and displacement for a single event (Figure 11). From their definition, the changes of $\tilde{\mu}$ and $\hat{\mu}$ can be considered as the variations in the logarithm of sliding velocity and in porosity, respectively.

Using the normalization approach suggested by Gu et al. (1984), the development of regular stick slips is illustrated in the phase plane of friction-velocity (Figure 12). When doing this, velocity is normalized by the imposed velocity, and friction coefficient is normalized as $(\mu - \mu_{ss})/a$, where the a value is calculated from the expression given in Paper 1, evaluated at the load point velocity. At the peak and trough friction points (annotated by **A**, **B**, and **C** for the second peak), the boundary friction coefficients ($\tilde{\mu}$) have the same value as the steady

state. This is intuitive since, at these points, the time derivatives of shear stress are zero ($\dot{\tau} = 0$) so that the velocities are the same as imposed slip rate ($V = V_{\text{imp}}$). After the peak stress has been attained (point **A**), the slip velocity increases monotonically to a maximum value, corresponding to the point of the maximum $\tilde{\mu}$ value (point **D**). Subsequently, the slip velocity decreases, passing through a point at which $\hat{\mu}$ reaches a minimum (point **E**) and then reaches the steady state value (point **B**). All along the “slip” phase of a stick-slip cycle (**A** \rightarrow **D** \rightarrow **E** \rightarrow **B**), the macroscopic shear strength drops quasi-statically. In contrast, during the stick phase (**B** \rightarrow **F** \rightarrow **G** \rightarrow **C** (or **A**)), the slip velocity first decreases and then increases, with the amplitude of the variation being smaller than in the slip phase. Correspondingly, $\tilde{\mu}$ decreases and then increases, reaching a minimum value at point **F**. All along the path, a maximum $\hat{\mu}$ value is achieved just before reaching the next peak point (**C** = **A**). As discussed above, the static stress drop ($\Delta\mu_s$) involved in a stick-slip event is determined by the difference in dilatant friction ($\hat{\mu}$) between the trough and peak points (**B** versus **C**). Therefore, $\Delta\mu_s$ is controlled by the amount of dilatancy during the slip phase (from **A** to **B**), which is recovered by compaction during the stick phase (from **B** to **C**).

Our quasi-static modeling shows that the slip rates achieved in the stick-slip events can be 4 to 5 orders of magnitude higher than the imposed velocity (cm/s, Figure 12). It is noteworthy that as slip rate increases, the

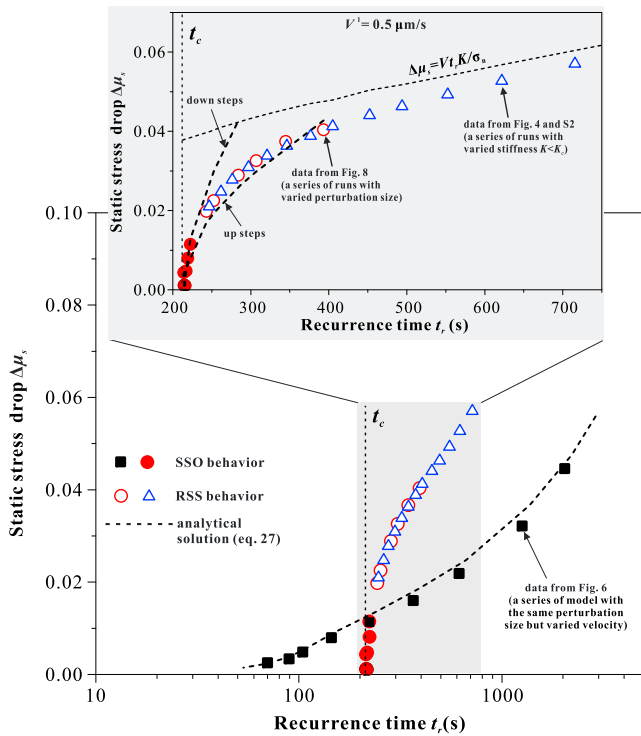


Figure 10. Modeling results showing static stress drop associated with SSO or RSS behavior ($\Delta\mu_s$) with respect to recurrence time (t_r). The squares are derived from the cases that have the same perturbation size ($V^1/V^0 = 0.5$) but variable loading rate; the circles are from the cases that have the same loading rate ($0.5 \mu\text{m/s}$) but with different sizes of the velocity steps; the triangles are derived from the cases that are run for the velocity step of $1.0 \rightarrow 0.5 \mu\text{m/s}$ but with varied stiffness. The solid and open circles indicate self-sustained oscillations (SSO) and regular stick slips (RSS), respectively.

inertial effect would become significant and suppress the dynamic velocity to be lower than the maximum velocity inherent to the quasi-static spring-slider system that is subjected to the same conditions (Gu & Wong, 1991; Rice & Tse, 1986). To understand how the mass of a fault plays a role in the framework of the microphysical model, numerical and theoretical studies including inertia are warranted in the future.

6.4. Forward RSF Modeling and Comparison

In the following, we perform forward RSF modeling using the parameters calculated from the expressions given in Paper 1 for a , b , and D_c , and in this study for K_c . The simulations are computed by the time integration of the spring-block fault system with friction governed by the RSF laws. The results are then compared with the direct predictions of the above implemented simulations using the CNS model. We use (1), (2a), and (2b) and combine $V_{\text{imp}} = \dot{\epsilon}/K + V$ as the governing equations. Both the Slowness law (2a) and Slip law (2b) are used as the state equations. The initial shear stress (τ^0) is set to be the steady state level at a prestep sliding rate (V^0) of $1 \mu\text{m/s}$. The initial state of the gouge (θ^0) is set to be D_c/V^0 , which puts the fault system in an initially stable sliding state. Similar to the CNS modeling, we simulate a velocity step test ($1.0 \rightarrow 0.5 \mu\text{m/s}$) under different apparatus stiffnesses. This modeling is again performed using the finite element package COMSOL.

Before comparing the simulation results, recall that previous stability analyses have shown that the Slowness and Slip laws give almost identical frictional response when subjected to small perturbations (e.g., Ruina, 1983), but they differ substantially in the presence of stick slips, either in the unstable regime ($K < K_c$) or in the stable regime but subjected to large size of perturbations (Gu et al., 1984; Ranjith & Rice, 1999). A related phenomenon was also noted by Beeler

et al. (1994) who observed that the predicted strength variations involved in slide-hold-slide tests are different for the Slowness and the Slip laws. Indeed, it is the dynamic response that distinguishes one friction law from another (Ampuero & Rubin, 2008; Bhattacharya & Rubin, 2014). As given in Paper 1, forward RSF modeling with the predicted a , b , and D_c values produces simulated friction behavior that is consistent with the predictions of the direct numerical implementation of the CNS model for small velocity steps, suggesting that these models are asymptotically identical in the vicinity of steady state. For large departures from steady state, that is, velocity steps of several orders of magnitude, the CNS model produces mixed RSF behavior between the Slowness and Slip laws, for example, with an intermediate slip(-weakening) distance. Note that in all of these exercises, stable sliding behavior is simulated ($K > K_c$).

Figure 13 presents the evolution of frictional strength from the RSF and CNS modeling under various spring stiffnesses. In the stable and neutral regimes ($K \geq K_c$), the frictional behavior predicted by the CNS model is consistent with that of faults with friction obeying the Slowness law or the Slip law, further confirming the validity of the CNS model (Figures 13a–13c). A notable example is under the “neutral stability” condition ($K = K_c$), where both the Slowness and Slip laws predict self-sustained oscillation behavior, with the recurrence intervals being consistent with the result obtained from the CNS model (Figure 13c). The amplitude of the oscillations predicted by the slip law is slightly smaller than that by the Slowness law or the CNS model. In the unstable regime ($K < K_c$), the prediction by the CNS model differs from that by the RSF laws (Figure 13d). The most remarkable difference is that the RSF laws predict oscillations that grow monotonically into infinity in finite time, while those predicted by the CNS model will either grow or attenuate into periodic behavior that has finite amplitude and recurrence interval (see more results from the CNS model in Figure S2).

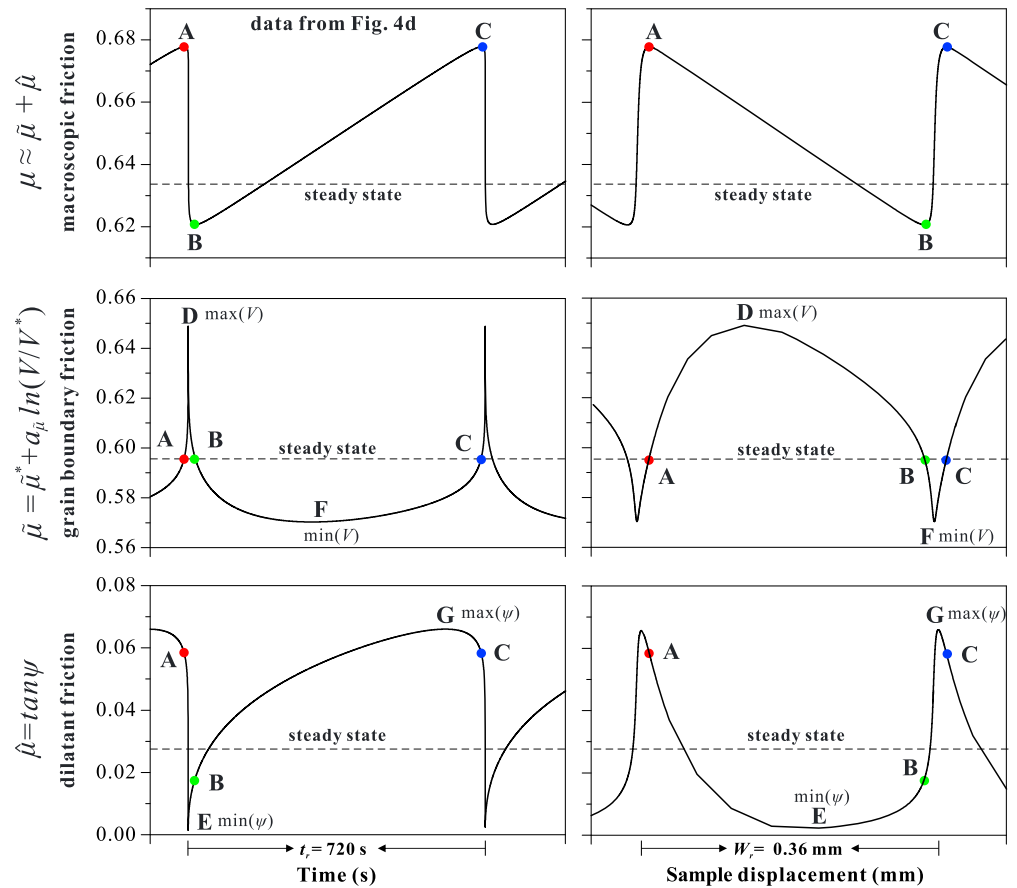


Figure 11. The evolution of friction during a stick-slip event with respect to shear time and sample displacement. The macroscopic friction coefficient is further decomposed into two components, namely, grain boundary friction and friction due to intergranular dilatation. The simulation was performed with a stiffness of $0.48 K_C$ and a velocity step from $1.0 \rightarrow 0.5 \mu\text{m/s}$ (see Figure 4d).

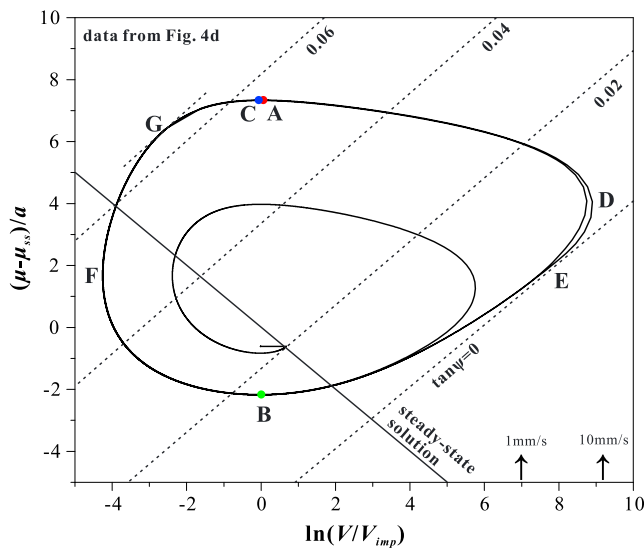


Figure 12. Stress-velocity phase plane plot of stick-slip cycles in the unstable regime. The same simulation as shown in Figure 11. The simulation was performed with a stiffness of $0.48 K_C$ and a velocity step from $1.0 \rightarrow 0.5 \mu\text{m/s}$.

7. Discussion

One would like to use the lab-derived frictional data to model natural earthquake dynamics. Given the physical expressions for the critical parameters associated with the slip stability (as summarized in Table 2), our model provides opportunities to address the following issues.

7.1. Overall Shear Strength Profile and Potentially Unstable Slip Regimes

The present model predicts a profile of steady state frictional/flow strength that passes through two transitions in its rate dependence as velocity increases: from velocity strengthening by plastic creep at low slip rates, via rate weakening in the intermediate slip rates, and then back to strengthening at high slip rates (Figures 2 and 3). As aforementioned, similar trends have been observed (sometimes partially) in many rocks or analogue materials such as quartz, calcite, serpentinite, halite, muscovite-quartz mixture, and natural clay-rich gouges (e.g., Shimamoto, 1986; Chester & Higgs, 1992; Niemeijer et al., 2016; see a review by Hawthorne & Rubin, 2013). Our theoretical analyses give the physical expressions for both transition velocities ($(35a)-(35c)$,

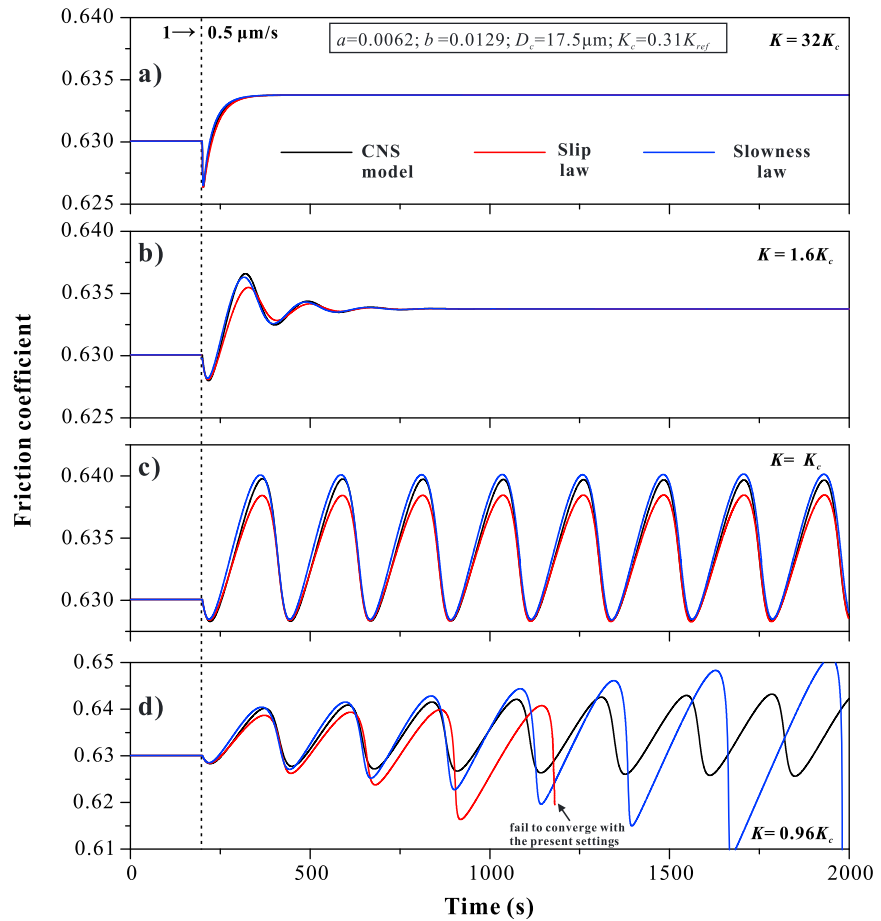


Figure 13. Comparison of the RSF and CNS modeling results showing friction coefficient versus time in the one-dimensional spring-slider elastic fault configuration. In all cases, the load point velocity is suddenly decreased from steady sliding at $1 \mu\text{m/s}$ to $0.5 \mu\text{m/s}$, subjected to the same normal stress but different host-rock stiffness K (shown in each subpanel). RSF parameters (a , b , and D_c) used in the RSF modeling are calculated from the analytical expressions given in Paper 1 and K_c from equation (19) of the present paper.

(37a), and (37b)) for $V_{s \rightarrow w}$ and $V_{w \rightarrow s}$, respectively) and the interval between these defines the potentially unstable slip regime.

To explain the flow-to-friction transition observed in serpentinites, Reinen et al. (1992) introduced a two-mechanism model, where two independent flow and friction laws are connected in an isostress fashion. Noda and Shimamoto (2010) connected the rate- and state-dependent flow/friction laws by adopting a hyperbolic tangent function, which allows a smooth transition from flow- to friction-governed rheology. Our model is distinguishable from the empirical or micromechanical laws (Chester & Higgs, 1992; Noda & Shimamoto, 2010; Putelat et al., 2007, 2010) because it provides a microphysical basis, that is, the transition occurs when a creeping gouge has to dilate and thereafter new brittle deformation mechanism(s) such as intergranular slip, microcracking, and/or strain localization starts to play a role (den Hartog & Spiers, 2014; Niemeijer & Spiers, 2007; Sleep, 1995).

Our model is in a sense distinct from these previous laws also because it predicts a second transition at higher velocities. This transition velocity is insightful for understanding the periodic oscillations observed in laboratory experiments (e.g., Gu & Wong, 1994; Leeman et al., 2016). As revealed by recent modeling work, the slip velocities associated with SSEs might be controlled by the transition velocity (Rubin, 2011; Shibasaki & Shimamoto, 2007). As given by equation (35c), we open a possibility to determine $V_{w \rightarrow s}$ from laboratory experiments, which might be relevant to the aseismic slip velocities characterizing the subduction zones (Hawthorne & Rubin, 2013). Meanwhile, cautions need to be taken since the maximum slip velocity

Table 1
 Explanation of Symbols Used in This Study

| Symbol | Description (unit) | Symbol | Description (unit) |
|---------------------|---|-----------------------|--|
| σ_n | effective normal stress (Pa) | t | time (s) |
| τ | shear stress (Pa) | t_c | critical recurrence time (s) |
| T | temperature (K) | t_r | recurrence time for SSO or RSS behavior (s) |
| μ | macroscopic or measured friction coefficient | t_0 | intercept of recurrence time (s) |
| μ_{ss} | steady state friction | V | slip velocity on the sample (m/s) |
| μ_{max} | maximum frictional strength | V_{imp} | imposed load point velocity (m/s) |
| $\tilde{\mu}$ | grain boundary (gb) friction coefficient | $V_{w \rightarrow s}$ | transition V from V weakening to strengthening |
| $\tilde{\mu}^*$ | reference gbs friction at a reference strain rate | $V_{s \rightarrow w}$ | transition V from V strengthening to weakening |
| $\hat{\mu}$ | friction due to intergranular dilatation ($\equiv \tan \psi$) | $\dot{\gamma}^*$ | a reference shear strain rate |
| $\hat{\mu}_{max}$ | maximum dilatant friction | L_t | thickness of the gouge layer (m) |
| $\Delta\mu_s$ | static stress drop with SSO or RSS behavior (Pa) ^a | λ | slip localization degree |
| ψ | dilatation angle | d | average grain size in shear band (m) |
| φ | porosity | H | geometrical parameter |
| φ_c | critical state (max) porosity for granular flow | q | two times critical porosity (φ_c) for shear band |
| φ_0 | terminal porosity of a compactional gouge | M | sensitivity of stress intensification to porosity |
| $\Delta\varphi_s$ | static porosity change with SSO or RSS behavior | N | sensitivity of dilatancy angle to porosity |
| a_c | average contact area (m ²) | A_n | geometric constant for compaction by IPS |
| $\dot{\epsilon}$ | compaction strain rate (s ⁻¹) | A_t | geometric constant for shear by IPS |
| $\dot{\gamma}$ | shear strain rate (s ⁻¹) | C | solubility of the solute in fluid film (m ³ /m ³) |
| κ | apparatus or natural fault stiffness (Pa/m) | Ω | molar volume of solid phase (m ³ /mol) |
| K_{ref} | a reference stiffness (5.993×10^{10} Pa/m) | DS | diffusion coefficient \times gb thickness (m ³ /s) |
| E | Young's modulus of surrounding fault rocks (Pa) | a | RSF parameter for direct effect |
| ν | Poisson's ratio of surrounding fault rock(s) | b | RSF parameter for evolution effect |
| K_c | critical stiffness (Pa/m) | θ | state variable in RSF laws (s) |
| K_r | stiffness when SSO or RSS behavior occurs (Pa/m) | D_c | characteristic slip distance in RSF laws (m) |
| W_c | critical wavelength (m) | L | length of asperity in natural faults (m) |
| W_r | wavelength when SSO or RSS behavior occurs (m) | $a_{\tilde{\mu}}$ | logarithmic rate dependence of gb friction |
| $\Delta\Phi_{\tau}$ | phase lag in shear stress with SSO or RSS behavior | b_{ψ} | logarithmic rate dependence of $\tan\psi$ |
| $\Delta\Phi_{\psi}$ | phase lag in state with SSO or RSS behavior | n | stress exponent of a power creep law |
| m | angle frequency of oscillations | | |
| Subscripts | | Superscripts | |
| pl | plastic contact creep mechanism | 0, 1 | reference/history state, new state |
| ss | steady state | sb | shear band |
| pk | peak point | bulk | bulk gouge |
| gr | granular flow | * | a reference case |
| s | (quasi-)static | | |

^aSSO and RSS denote self-sustained oscillations and regular stick slips, respectively.

attained during the SSEs is controlled not only by the transition velocity but also by the departure from the critical stiffness, that is, by the amount of energy available for acceleration. Finally, porosity is the state variable of the CNS model and it increases with increasing slip rate (Figure 3), as observed in many previous experiments (e.g., Marone et al., 1990). Therefore, our model can provide a physical interpretation of the empirical relations previously proposed to link velocity and the dynamic porosity of a shearing gouge (e.g., Segall & Rice, 1995; Sleep, 1995). It seems natural and also promising to incorporate dilatant hardening into the model to explain slow slips (Liu & Rubin, 2010; Segall et al., 2010).

7.1.1. Evolution of Friction With Depth

Similar transitions with slip rate as given in Figure 3 can be also predicted by the model with increasing temperature, since a decrease of slip velocity is to some extent equivalent to an increase in temperature (e.g., Bos & Spiers, 2002; Niemeijer & Spiers, 2005, 2007). As applied to natural faults, with increasing depth,

Table 2
 Microphysical Interpretation of the Slip Stability Parameters

| Symbol | Expression | Equivalent form | Reference |
|-----------------------|---|---|---------------------------|
| K_c | $\frac{2HN(M+N)(1-\varphi_{ss})\sigma_n}{L_t\lambda} \left[b_\psi \frac{(1+\tilde{\mu}_{ss}^2)}{(1-\tilde{\mu}_{ss}\hat{\mu}_{ss})^2} - a_\mu \frac{(1+\hat{\mu}_{ss}^2)}{(1-\tilde{\mu}_{ss}\hat{\mu}_{ss})^2} \right]$ | $\frac{(b-a)\sigma_n}{D_c}$ | Equation (19) or (29) |
| W_c | $\frac{\pi L_t\lambda}{HN(M+N)(1-\varphi_{ss})\sqrt{\frac{b_\psi(1+\tilde{\mu}_{ss}^2)}{a_\mu(1+\hat{\mu}_{ss}^2)} - 1}}$ | $2\pi D_c \sqrt{\frac{a}{b-a}}$ | Equation (21) or (31) |
| $\Delta\mu_s$ | $2\sqrt{b_\psi \frac{(1+\tilde{\mu}_{ss}^2)}{(1-\tilde{\mu}_{ss}\hat{\mu}_{ss})^2} \left[b_\psi \frac{(1+\tilde{\mu}_{ss}^2)}{(1-\tilde{\mu}_{ss}\hat{\mu}_{ss})^2} - a_\mu \frac{(1+\hat{\mu}_{ss}^2)}{(1-\tilde{\mu}_{ss}\hat{\mu}_{ss})^2} \right] \left \ln\left(\frac{V^1}{V^0}\right) \right }$ | $2\sqrt{b(b-a)} \left \ln\left(\frac{V^1}{V^0}\right) \right $ | Equation (27) |
| $V_{w \rightarrow s}$ | $\frac{L_t\lambda E_{pl}(T, d, \sigma_n)}{H} \left[\frac{H(1+\tilde{\mu}^{+2})}{a_\mu(M+N)} \right]^{(M+N)}$ | $V^* \left(\frac{b}{a}\right)^{(M+N)}$ | Equations (35a)–(35c) |
| $V_{s \rightarrow w}$ | $\frac{L_t\lambda E_{pl}(T, d, \sigma_n)}{H(q-2\varphi_0)^{N(M+N)}}$ | $V^* \left(\frac{\varphi_c - \varphi_0}{\varphi_c - \varphi_0}\right)^{N(M+N)}$ | Equations (37a) and (37b) |

Note. K_c : critical stiffness; W_c : critical recurrence interval; $\Delta\mu_s$: static friction drop; $V_{w \rightarrow s}$: cutoff velocity from velocity weakening to strengthening; $V_{s \rightarrow w}$: transition velocity from flow to friction. In these expressions, $\tilde{\mu}$ is grain boundary friction and $\hat{\mu} \equiv \tan\psi$ is defined as dilatant friction coefficient, and $a_\mu = \frac{\partial \tilde{\mu}}{\partial(\ln V)} = \frac{kT}{\sigma_l \Omega_l}$ and $b_\psi = \frac{\partial \hat{\mu}}{\partial(\ln V)} = \frac{\hat{\mu}}{M+N}$ specifying the logarithmic rate dependences of $\tilde{\mu}$ and $\hat{\mu}$, respectively. The expressions for a , b , and D_c and for the steady state parameters, namely, φ_{ss} , $\tilde{\mu}_{ss}$, $\hat{\mu}_{ss}$, and μ_{ss} , are given in Paper 1. Others like $L_t\lambda$, d , H , M , N , $q(=2\varphi_c)$ and φ_0 are material or fault structural parameters, T and σ_n are external fault conditions, and E_{pl} is a general creep law as a function of T , d , and σ_n . Note that the expressions of $V_{w \rightarrow s}$ and $V_{s \rightarrow w}$ given above are derived using a general creep law (E_{pl}) and with general M and N values, while the ones given in the main text use a linear creep law and with specific M and N values ($M = 2$ and $N = 1$).

the increased temperature and effective normal stress will enhance compaction creep process, leading to larger dilatancy angles and thus larger evolution effects. According to the strain rate sensitivity of grain boundary friction that is $a_\mu = \frac{kT}{\sigma_l \Omega_l}$, the changes in temperature and pressure will change the direct effect but in an opposite direction. With distinct sensitivities with respect to depth, the combination of both effects will give rise to a transition from velocity strengthening to velocity weakening with increasing depth. Farther downdip, as the fault rheology enters the flow regime, it will turn back to velocity strengthening. Recently, van den Ende et al. (2017) implemented the CNS model in a seismic cycle simulator to model the dynamics of an upper crustal strike-slip fault, assuming quartz as the constitutive mineral of the fault gouge, for which dissolution-controlled IPS is considered to be the dominant creep mechanism. With reasonable geothermal and pressure gradients as inputs, their model predicts the same transitions in the friction rate dependence with depth.

Finally, it is important to note that the steady state shear strength, as well as the rate-sensitivity parameter ($a - b$) predicted by the CNS model, vary not only with slip velocity and temperature (depth) as discussed above but also with other factors such as grain size and strain localization. This is distinct from the classical RSF laws in which the constitutive parameters are usually taken as constants. As a consequence, the seismogenic zone, as defined by the velocity-weakening regime (Scholz, 2002), shows spatiotemporal variations over a seismic cycle, while in the classical RSF framework, is defined by a negative ($a - b$), which is imposed a priori.

7.2. Variable Critical Stiffness (K_c) and Implications for a Seismogenic Fault

Our numerical modeling demonstrates that in the potentially unstable slip regime, as the fault stiffness decreases, slip motion of a velocity-weakening fault under quasi-static loading shows a transition from stable sliding, via attenuated or self-sustained oscillations, to regular stick slips (Figure 4). These features are in general agreement with those observed in previous experiments (e.g., Wong & Zhao, 1990) and with the predictions from the RSF laws (Gu & Wong, 1994; Rice & Tse, 1986). Expression (19) further gives that critical stiffness

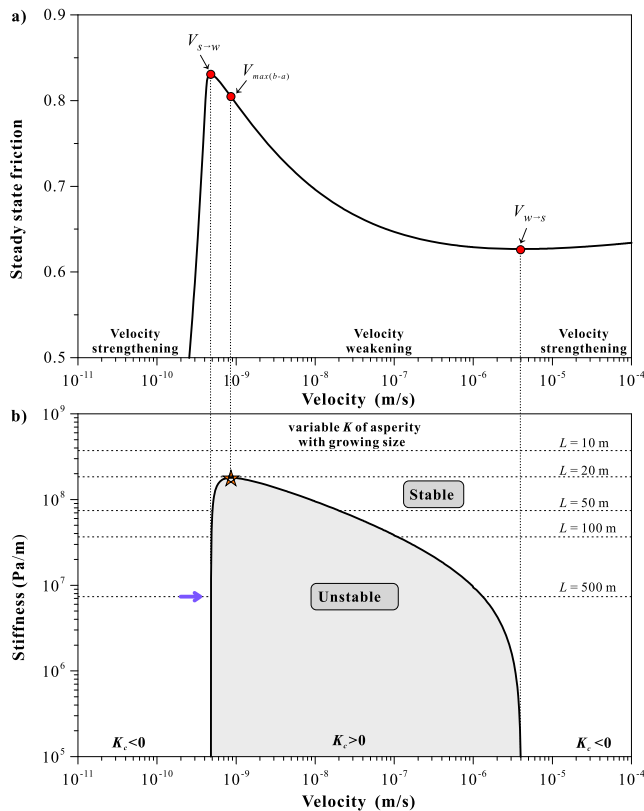


Figure 14. Plot showing the slip stability spectrum predicted by the microphysical model. (a) Steady state friction curves with sliding velocity for a simulated carbonate fault sheared at 80°C hydrothermal conditions, where diffusion-controlled pressure solution is inferred to be the contact creep mechanism (Chen & Spiers, 2016) (the same implementation as Figure 3). (b) Critical stiffness K_c is calculated using equation (19) with an effective normal stress of 50 MPa. Other properties in expressing K_c are derived from the lab-simulated carbonate fault. The effective fault stiffness K is computed for a circular slip patch embedded in an elastic half-space, with growing diameter with time (the dashed lines showing the K value for slip regions of 10, 20, 50, and 100 m in diameter). Under these range of conditions, a transition from stable to unstable fault motion would first emerge at a slip rate of $\sim 9 \times 10^{-10}$ m/s if, at the same time, the dislocation patch has grown into a diameter of larger than ~ 20 m (indicated by the red star).

(K_c) scales with effective normal stress (σ_n) and the grain geometric constant (H) and is inversely proportional to D_c and thus slip band thickness (L_{tj}), as discussed in the following.

With increasing effective normal stress (σ_n) or decreasing shear band thickness (L_{tj}), a transition from stable to unstable frictional behavior is predicted by the CNS model (not presented in this study). The fact that higher effective normal stress favors the occurrence of unstable slip has been widely observed in previous experiments (e.g., Byerlee and Brace, 1968; Scholz, 2002). The effects of shear band thickness on the stability of a fault involve slightly more complexity. On the one hand, according to the shear strength profile predicted (Figure 3), slip (de)localization will cause variations in the friction rate dependence. On the other hand, based on the expression derived, D_c is proportional to L_{tj}^λ , consistent with the interpretations from previous experiments (e.g., Marone and Kilgore, 1993). Slip localization will cause a decrease in D_c and an increase in K_c , leading to a trend toward unstable behavior, while delocalization will stabilize fault slip. This is consistent with the recognition from previous experimental studies that unstable slip can be inhibited by gouge production from wearing (e.g., Byerlee & Summers, 1976) and that unstable slip tends to be promoted by slip localization (e.g., Leeman et al., 2016; Niemeijer et al., 2010). The H value primarily depends on the grain shape and grain size distribution of the gouge and is not well constrained in our model. The recent implementation of the CNS model by van den Ende et al. (2017) shows that with a larger H value, the fault slip behavior becomes less stable compared with a gouge with a smaller H value when subjected to otherwise identical conditions, that is, stick slips have larger stress drop and larger maximum slip velocity.

As an equivalent form of (19), equation (29) indicates that the critical stiffness also scales with the rate dependence of steady state friction coefficient ($a - b$). However, different from RSF laws, our model predicts that ($a - b$) is itself rate dependent. As driving velocity decreases (or temperature increases), the fault motion will exhibit a transition from velocity strengthening to velocity weakening (Figure 14a). In the velocity-weakening regime, lower loading rate corresponds to more negative ($a - b$). This feature is confirmed by our numerical modeling results that show larger-amplitude stick slips at lower velocities

(Figure 6), and it is also consistent with the observations in previous experimental studies (e.g., Anthony & Marone, 2005; Cao & Aki, 1986; McLaskey et al., 2012). Other parameters such as the grain size, the geometrical, and material properties (d , α_μ , $\tilde{\mu}^*$, φ_c , H , C , M , and N values) can also affect the critical stiffness but all through changing ($a - b$). The variations of ($a - b$) with these parameters and between different materials under variable conditions are discussed in detail in Paper 1. For instance, smaller grain size produces faster compaction creep rates, which lead to larger evolution effects and thus more negative values of ($a - b$), prone to unstable behavior. The same trend applies to fault gouges consisting of minerals that have faster kinetics of pressure solution (e.g., calcite versus quartz), or of the same mineral but subjected to hydrothermal versus dry conditions (different M values and/or creep laws). Note that here the H value plays a second important role. A larger H value produces a more negative ($a - b$), again favoring the occurrence of unstable slip.

Conclusively, among all the parameters discussed above, critical stiffness exhibits a strong dependence on the extent of slip localization, the normal stress, the driving velocity, the temperature, the grain size, the H value, and the creep kinetics but little dependence on the reference grain boundary friction coefficient $\tilde{\mu}^*$ and the critical porosity φ_c .

As applied to earthquake faults, the expression of K_c as a function of σ_n , V_{imp} , and λ indicates that there is a high potential for a highly stressed, slowly driven, and well-localized fault to generate substantially unstable frictional behavior. However, as the sliding velocity decreases further, the ductile/plastic shear creep will become increasingly important, giving rise to a transition to the velocity strengthening regime (Figure 14a). This makes the overall profile of slip stability with respect to sliding velocity complicated (Figure 14b). A positive critical stiffness only exists in the intermediate velocity regime, where the fault shows velocity-weakening behavior. The profile suggests that at a given effective normal stress (depth), there may exist a specific velocity at which the value of $(b - a)$ and thus the critical stiffness reaches the maximum (see the star in Figure 14b). As a first-order estimate, one can, therefore, predict a transition from potentially stable to unstable slip, based on the point at which the local stiffness K around a growing dislocation (or asperity or slip patch) drops below the critical stiffness (e.g., Gu et al., 1984; Roy & Marone, 1996). In Figure 14b, we provide one example to illustrate this. On the one hand, the critical stiffness K_c as a function of slip rate is calculated for a carbonate fault zone at a depth of ~ 4 km ($\sigma_n = 50$ MPa and $T = 80^\circ\text{C}$), using expression (19) with properties derived from experiments performed at similar conditions (the same as our numerical implementation in section 6). On the other hand, the effective stiffness of a fault K is specified by elastic constants of the constitutive rock(s) and is inversely proportional to a length scale (Scholz, 2002):

$$K = \frac{E}{2(1 - \nu^2)L}, \quad (40)$$

where E and ν are Young's modulus and Poisson's ratio of the surrounding rocks (7 GPa and 0.25), respectively, and L is the length of the asperity (or slip patch). Here the local effective stiffness K is computed assuming a circular slip patch (or elliptical crack) embedded in an elastic half-space, the diameter of which grows with time (Gu et al., 1984; Marone & Saffer, 2015). According to (40), the K value decreases with increasing diameter (Figure 14b). Let us then assume that the carbonate fault has entered a seismic cycle and the slip rate on this patch is accelerating in the preseismic phase. As the slip reaches the specific velocity at which the gouge has the minimum $(a - b)$ value (at $\sim 9 \times 10^{-10}$ m/s in the case shown in Figure 14b), the fault zone would have the highest critical stiffness, corresponding to the highest potential for the nucleation of an earthquake. If the slip patch has, concomitantly, grown from a small size to be larger than 20 m in diameter, unstable frictional behavior is expected to occur; or if the patch is initially large (say 500 m in diameter, as indicated by the blue arrow in Figure 14b), the unstable slip could occur earlier and at slightly smaller slip rate ($\sim 5 \times 10^{-10}$ m/s).

The example given in Figure 14 shows that concomitant changes in slip velocity and the size of the slip region may play a central role in determining the transition of a fault from stable to unstable frictional behavior. According to our model, the unstable slip region (seismogenic zone) in a natural fault would experience spatial and temporal variations within the seismic cycle. This feature is much more complicated than previous interpretations based on the RSF laws, in which the minimum length scale for earthquake nucleation at a given depth (effective normal stress) is constant (Scholz, 2002). This warrants numerical simulations of realistic earthquake cycles using our CNS model in the future.

7.3. Static Stress Drop ($\Delta\mu_s$) and Recurrence Time (t_r)

7.3.1. Scaling of $\Delta\mu_s$ With Frictional Parameter

Our linearized analysis gives the expression for the static stress drops associated with the SSO and RSS behaviors in the neutral stability regime, that is, $\Delta\mu_s = 2\sqrt{b(b - a)} |\ln(V^1/V^0)|$. The equation indicates that $\Delta\mu_s$ scales with $\sqrt{b(b - a)}$ and the logarithm of velocity perturbation size ($|\ln(V^1/V^0)|$), which is confirmed by our numerical modeling results (Figures 9b and 9c). Our model also predicts a negative dependence of $\Delta\mu_s$ on the driving velocity V^1 (Figure 9a). Based on numerical simulations with friction governed by the RSF laws, an empirical scaling relation has been previously established by Gu and Wong (1991): $\Delta\mu_s = (b - a)[2|\ln(V^1/V^0)| + C]$, where C is a parameter that is independent of velocity (see also He et al., 2003). This relation shows that $\Delta\mu_s$ is linearly related to the velocity weakening parameter $(b - a)$. With insights gained from their simulations, these authors found that the C value decreases with increasing stiffness, and at a neutral stability condition ($K = K_c$), the friction oscillation amplitude should diminish to zero ($C = 0$) if the perturbation is small. The $\Delta\mu_s$ data obtained from our simulations are plotted against $(b - a) |\ln(V^1/V^0)|$ (Figure S3). Surprisingly, our data also fit reasonably well with this equation, with very small C value.

The difference between our and Gu and Wong's equations lies in the proportionality factor, $(b - a)$ versus $\sqrt{b(b - a)}$. We note that these two quantities are linearly related to one another if $b > 1.25a$ (Figure S4). Coincidentally, Gu and Wong observed that the scaling relation they proposed does not apply for constitutive parameters with $b/a < 1.2$. Considering that the scaling relation we report here is rigorously derived and has a microphysical basis, we believe that it is more robust. However, it should be noted that our relation only applies to the neutral condition. In the unstable regime ($K < K_c$), our preliminary modeling results exhibit a tendency for $\Delta\mu_s$ to increase with decreasing stiffness (Figure S2). For a robust scaling relation that describes the static stress drops ($\Delta\mu_s$) as functions of slip velocity, perturbation size, and stiffness, more work is needed.

7.3.2. Scaling of $\Delta\mu_s$ With Time

Our modeling results demonstrate that the relation of $\Delta\mu_s$ versus $\log(t_r)$ exhibits two trends with distinct slopes (Figure 10). Similar trends are visible in the compiled data set of previous experimental results (e.g., McLaskey et al., 2012; Scuderi et al., 2014; Wong & Zhao, 1990). For the low slope trend (Figure 10), in which the data were usually derived from experiments with variable loading rates (see Figure 4 in Karner & Marone, 2000; Figure 8a in Beeler et al., 2014; Figure 10 in Scuderi et al., 2014; and Figure 4 in Leeman et al., 2014), Beeler et al. (2014) proposed an empirical relation of the logarithm form: $\Delta\mu_s \propto \ln(t_r/t_0)$, where t_0 is the intercept of recurrence interval at zero stress drop. Here our model predicts a similar trend but not in a log linear relation (Figure 9a). Based on the theoretical expression derived, the varying slope reflects the variation in the rate dependence of $\sqrt{b(b - a)}$. The large slope trend represents the variation of $\Delta\mu_s$ with recurrence time at a given (constant) slip rate. In experimental studies, this trend was inferred to reflect the variations of material strength between different stick-slip events (Karner & Marone, 2000; Leeman et al., 2014; Scuderi et al., 2014). Here our model shows that the trend may come from the variations in perturbation size or stiffness. The $\Delta\mu_s$ data in this trend also appear to follow a linear relation with t_r , that is $\Delta\mu_s \propto t_r$, especially for large stick slips (inset of Figure 10). This is again consistent with previous experimental results (e.g., Figure 6a in Karner & Marone, 2000). Assuming that stick accounts for most of the recurrence time, this linear relation can be expressed as an asymptotic line: $\Delta\mu_s = \frac{KV_{\text{imp}}}{\sigma_n} t_r$ (e.g., Beeler et al., 2014).

Note that in the present study, we have neglected the mass of the spring-slider fault system. The inertia will become important if the acceleration is significant, for example, during stick-slip events where the maximum slip rate can be several orders of magnitude higher than the imposed one, as is also the case for our simulations (Figure 12). When inertia is considered, the evolution of shear stress during a stick slip could be modified by a dynamic damping; part of the stress drop that corresponds to dynamic slip is termed "dynamic stress drop" (Rice & Tse, 1986; Roy & Marone, 1996). However, for a single-state-variable system, the overall characteristics of stick slips with inertia are similar to the quasi-static case (Rice & Tse, 1986). Therefore, our discussions on static stress drop as above are still valid.

7.4. Regular Stick Slips Characteristic to the Microphysical Model

In the context of RSF laws, to achieve regular stick slips or self-sustained oscillations, it is necessary for the stiffness of a fault to be close to the critical stiffness ($K \approx K_c$), while in the unstable regime ($K < K_c$), the stick slips will grow in size with slip speed becoming unbounded in finite time (Gu et al., 1984; Ranjith & Rice, 1999). In previous analyses of the dynamics of a spring-slider system obeying the RSF laws, either a second state variable, or inertia, and/or some limiting speed procedure (e.g., a cutoff velocity) was introduced for such a system to produce characteristic earthquakes (Becker, 2000; Cao & Aki, 1986; Gu et al., 1984; Gu & Wong, 1991). The inertial effect of a nonzero mass can be taken as another degree of freedom, and including a mass into the linear stability analysis of a spring-slider system can result in a change in the critical stiffness (Rice & Ruina, 1983). However, this kind of mediation is not always plausible for laboratory experiments, since in some tests these effects (a second state variable and inertia) were clearly negligible (e.g., Baumberger et al., 1994; Noda & Shimamoto, 2010; Scuderi et al., 2014; Leeman et al., 2014, 2016).

Our preliminary results show that in the unstable regime ($K < K_c$), regular stick slips can be predicted by the CNS model without resorting to any speed-limiting modification. During the stick slips, the slip velocity does not have the unbounded-velocity problem as in the RSF laws (Figure 13d, Gu et al., 1984), which means that the slip velocity does not evolve into infinity in finite time (Figures 12 and 13d). This suggests that our model has a supercritical Hopf bifurcation characteristic, at least for the calcite gouge material at the simulated

condition. To further gain insight from this observation, nonlinear stability analyses of a fault system need to be done in the future.

Finally, in the stick slip events predicted by the model, the gouge compacts during the stick phase and dilates for the slip period (see Figure 11 and note that porosity evolves in the opposite direction of $\hat{\mu}$). Similar behavior has been observed in laboratory experiments for material with high rates of compaction (relative to the load point velocity), such as the Alpine fault gouges (Niemeijer et al., 2016). It is noteworthy that an opposite compaction/dilatation behavior associated with stick slips has been observed for granular material such as dry quartz and glass beads (Anthony & Marone, 2005; Doanh et al., 2013; Scuderi et al., 2015). This behavior has been explained in a framework of force-chain formation and collapse (Anthony & Marone, 2005), which differs from our model. The stick-slip cycles generated by our microphysical model show parallels with classical seismic cycle models, where faults are believed to compact during the interseismic phase and consequently dilate during the coseismic phase (e.g., Segall & Rice, 1995; Sibson, 1990). Moreover, our model predictions are also consistent with previous SHS experiments that show continuous compaction during the hold phase and dilatation upon resliding (Bos & Spiers, 2002; Chen et al., 2015a; Niemeijer et al., 2008; Yasuhara et al., 2005).

8. Summary and Conclusions

In the present study and a companion paper, we have examined a microphysical friction model proposed by Chen and Spiers (2016) and Niemeijer and Spiers (2007), by performing theoretical and numerical analyses on the model and comparing the predictions with the classical RSF laws. In this study, we focused on the slip stability of the model.

In a spring-slider configuration under constant normal stress, linearized stability analysis yields the expressions for the critical stiffness (K_c), the characteristic recurrence wavelength (W_c), and the static stress drops ($\Delta\mu_s$) associated with the regular stick slips or self-sustained oscillations. The same K_c and W_c are obtained by an independent approach, that is, Rice and Ruina's theory, using expressions for RSF parameters given in the companion paper. Considering a simulated carbonate fault gouge sheared at hydrothermal conditions, numerical implementation of our model indicates that as the stiffness of the surrounding of the fault decreases, the fault motion transitions from stable sliding via self-sustained oscillations, to unstable slip behavior (stick slips with limit cycles), with critical quantities (K_c , W_c and $\Delta\mu_s$) that are consistent with the predictions from the analytical expressions. In particular, critical stiffness K_c is proportional to effective normal stress, inversely proportional to shear band thickness, and increases with decreasing loading rate; W_c also scales with shear band thickness. The static stress drop $\Delta\mu_s \propto \sqrt{b(b-a)} |\ln(V^1/V^0)|$ at nearly neutral conditions, while for large-amplitude stick slips, it is roughly proportional to recurrence time ($\Delta\mu_s \propto t_r$). All the expressions derived (i.e., K_c , W_c and $\Delta\mu_s$) are in broad agreement with previous recognitions obtained in the context of RSF laws. Forward RSF modeling further confirms this point.

The model predicts a steady state frictional/flow profile, exhibiting consecutive transitions from velocity strengthening at low slip rates, via velocity weakening at intermediate slip rates, back to velocity strengthening at high slip rates. The analytical solutions for this profile are given in the companion paper. In this study, the two critical velocities that divide these transitions, $V_{s \rightarrow w}$ and $V_{w \rightarrow sr}$, are theoretically obtained, and the interval between these defines the unstable slip regime, which is confirmed by the numerical results. The latter one, $V_{w \rightarrow sr}$, has been recognized to be important for understanding the periodic oscillations and slow-slip events observed in both laboratory and natural faults. Our derived expression opens the possibility to determine the slow-slip velocities characterizing subduction fault zones from laboratory experiments.

Acknowledgments

We thank the Associate Editor Y. Kaneko and two anonymous reviewers for detailed and insightful reviews. We acknowledge M. P. A. van den Ende and J. -P. Ampuero for fruitful discussions. Jianye Chen is funded by the European Research Council starting grant SEISMIC (335915). André Niemeijer is funded by SEISMIC (335915) and the Netherlands Organisation for Scientific research (NWO) VIDI grant (854.12.011). This is a theoretical paper, and it does not contain any data.

References

- Ampuero, J.-P., & Rubin, A. M. (2008). Earthquake nucleation on rate and state faults: Aging and slip laws. *Journal of Geophysical Research*, *113*, B01302. <https://doi.org/10.1029/2007JB005082>
- Anthony, J. L., & Marone, C. (2005). Influence of particle characteristics on granular friction. *Journal of Geophysical Research*, *110*, B08409. <https://doi.org/10.1029/2004JB003399>
- Baumberger, T., Heslot, F., & Perrin, B. (1994). Crossover from creep to inertial motion in friction dynamics. *Nature*, *367*, 544–546.
- Becker, T. W. (2000). Deterministic chaos in two state-variable friction sliders and the effect of elastic interactions. In J. B. Rundle, D. L. Turcotte, & W. Klein (Eds.), *Geocomplexity and the Physics of Earthquake* (pp. 5–26). Washington, DC: American Geophysical Union.

- Beeler, N. M. (2004). Review of the physical basis of laboratory-derived relations for brittle failure and their implications for earthquake occurrence and earthquake nucleation. *Pure and Applied Geophysics*, 161, 1853–1876.
- Beeler, N. M., Tullis, T., Junger, J., Kilgore, B., & Goldsby, D. (2014). Laboratory constraints on models of earthquake recurrence. *Journal of Geophysical Research: Solid Earth*, 119, 8770–8791. <https://doi.org/10.1002/2014JB011184>
- Beeler, N. M., Tullis, T. E., & Weeks, J. D. (1994). The roles of time and displacement in the evolution effect in rock friction. *Geophysical Research Letters*, 21, 1986–1990.
- Berthoud, P., Baumberger, T., G'Sell, C., & Hiver, J.-M. (1999). Physical analysis of the state- and rate-dependent friction law: Static friction. *Physical Review B*, 59(22), 14,313–14,327.
- Bhattacharya, P., & Rubin, A. M. (2014). Frictional response to velocity steps and 1-D fault nucleation under a state evolution law with stressing-rate dependence. *Journal of Geophysical Research*, 119, 2272–2304.
- Bos, B., & Spiers, C. J. (2002). Fluid-assisted healing processes in gouge bearing faults: Insights from experiments on a rock analogue system. *Pure and Applied Geophysics*, 159, 2537–2566.
- Buijze, L., Niemeijer, A., Han, R., Shimamoto, T., & Spiers, C. J. (2017). Friction properties and deformation mechanisms of halite(-mica) gouges from low to high sliding velocities. *Earth and Planetary Science Letters*, 458, 107–119.
- Byerlee, J. D. (1970). The mechanics of stick-slip. *Tectonophysics*, 9, 475–486.
- Byerlee, J. D., & Brace, W. F. (1968). Stick slip, stable sliding, and earthquakes – effect of rock type, pressure, strain rate, and stiffness. *Journal of Geophysical Research*, 73, 6031–6037.
- Byerlee, J. D., & Summers, R. (1976). A note on the effect of fault gouge thickness on fault stability. *International Journal of Rock Mechanics and Mining*, 13, 35–36.
- Cao, T., & Aki, K. (1986). Effect of slip rate on stress drop. *Pure and Applied Geophysics*, 124, 515–530.
- Chen, J., Niemeijer, A. R., & Spiers, C. J. (2017). Microphysically derived expressions for rate-and-state friction parameters, a , b , and D_c . *Journal of Geophysical Research: Solid Earth*, 122, 9627–9657. <https://doi.org/10.1002/2017JB014228>
- Chen, J., & Spiers, C. J. (2016). Rate and state frictional and healing behavior of carbonate fault gouge explained using microphysical model. *Journal of Geophysical Research*, 121, 8642–8665.
- Chen, J., Verberne, B. A., & Spiers, C. J. (2015a). Interseismic re-strengthening and stabilization of carbonate faults by “non-Dieterich” healing under hydrothermal conditions. *Earth and Planetary Science Letters*, 423, 1–12.
- Chen, J., Verberne, B. A., & Spiers, C. J. (2015b). Effects of healing on the seismogenic potential of carbonate fault rocks: Experiments on samples from the Longmenshan Fault, Sichuan, China. *Journal of Geophysical Research*, 120, 5479–5506.
- Chester, F. M., Evans, J. P., & Biegel, R. L. (1993). Internal structure and weakening mechanisms of the San Andreas Fault. *Journal of Geophysical Research*, 98, 771–786.
- Chester, F. M., & Higgs, N. G. (1992). Multimechanism friction constitutive model for ultrafine quartz gouge at hypocentral conditions. *Journal of Geophysical Research*, 97(B2), 1859–1870.
- De Bresser, J. H. P., Evans, B., & Renner, J. (2002). On estimating the strength of calcite rocks under natural conditions. In S. De Meer, et al. (Eds.), *Deformation Mechanisms, Rheology and Tectonics: Current Status and Future Perspectives*, Geological Society, London Special Publication, (Vol. 200, pp. 309–329).
- den Hartog, S., & Spiers, C. J. (2014). A microphysical model for fault gouge friction applied to subduction megathrusts. *Journal of Geophysical Research*, 119, 1510–1529. <https://doi.org/10.1002/2013JB010580>
- Dieterich, J. H. (1979). Modeling of rock friction: 1. Experimental results and constitutive equations. *Journal of Geophysical Research*, 84(B5), 2161–2168.
- Dieterich, J. H., & Linker, M. F. (1992). Fault stability under conditions of variable normal stress. *Geophysical Research Letters*, 19(16), 1691–1694.
- Doanh, T., Hoang, M. T., Roux, J.-N., & Dequeker, C. (2013). Stick-slip behavior of model granular materials in drained triaxial compression. *Granular Matter*, 15, 1–23.
- Gu, J. C., Rice, J. R., Ruina, A. L., & Tse, S. T. (1984). Slip motion and stability of a single degree of freedom elastic system with rate and state dependent friction. *Journal of the Mechanics and Physics of Solids*, 32, 167–196.
- Gu, Y., & Wong, T.-f. (1991). Effects of loading velocity, stiffness, and inertia on the dynamics of a single degree of freedom spring-slider system. *Journal of Geophysical Research*, 96, 21,677–21,691.
- Gu, Y., & Wong, T.-f. (1994). Nonlinear dynamics of the transition from stable sliding to cyclic stick-slip in rock. In W. I. Newman, A. M. Gabrielov, & D. L. Turcotte (Eds.), *Nonlinear Dynamics and Predictability of Geophysical Phenomena*, Geophysical monograph (Vol. 83, pp. 15–35). Washington, DC: American Geophysical Union.
- Hatano, T. (2015). Rate and state friction law as derived from atomistic processes at asperities, *Statistical Mechanics*. <https://doi.org/arXiv:1512.05078> [cond-mat.stat-mech].
- Hawthorne, J. C., & Rubin, A. M. (2013). Laterally propagating slow slip events in a rate and state friction model with a velocity-weakening to velocity-strengthening transition. *Journal of Geophysical Research: Solid Earth*, 118, 3785–3808. <https://doi.org/10.1002/jgrb.50261>
- He, C., Wong, T.-f., & Beeler, N. M. (2003). Scaling of stress drop with recurrence interval and loading velocity for laboratory derived fault strength relations. *Journal of Geophysical Research*, 108(B1), 2037. <https://doi.org/10.1029/2002JB001890>
- Hirose, H., Hirahara, K., Kimata, F., Fujii, N., & Miyazaki, S. (1999). A slow thrust slip event following the two 1996 Hyuganada earthquakes beneath the Bungo Channel, southwest Japan. *Geophysical Research Letters*, 26(21), 3237–3240.
- Ikari, M. J., Carpenter, B. M., & Marone, C. (2016). A microphysical interpretation of rate- and state-dependent friction for fault gouge. *Geochemistry, Geophysics, Geosystems*, 17, 1660–1677.
- Karner, S. L., & Marone, C. (2000). Effects of loading rate and normal stress on stress drop and stick-slip recurrence interval. In J. B. Rundle et al. (Eds.), *Geocomplexity and physics of earthquakes* (pp. 187–198). Washington, DC: American Geophysical Union.
- Lapusta, N., Rice, J. R., Ben-Zion, Y., & Zheng, G. (2000). Elastodynamic analysis for slow tectonic loading with spontaneous rupture episodes on faults with rate- and state-dependent friction. *Journal of Geophysical Research*, 105(B10), 23,765–23,789.
- Leeman, J., Scuderi, M., Marone, C., Saffer, D. M., & Shinbrot, T. (2014). On the origin and evolution of electrical signals during frictional stick slip in sheared granular material. *Journal of Geophysical Research: Solid Earth*, 119, 4253–4268. <https://doi.org/10.1002/2013JB010793>
- Leeman, J. R., Saffer, D. M., Scuderi, M. M., & Marone, C. (2016). Laboratory observations of slow earthquakes and the spectrum of tectonic fault slip modes. *Nature Communications*, 7. <https://doi.org/10.1038/ncomms11104>
- Linker, M. F., & Dieterich, J. H. (1992). Effects of variable normal stress on rock friction: Observations and constitutive equations. *Journal of Geophysical Research*, 97(B4), 4923–4940.
- Liu, Y., & Rice, J. R. (2007). Spontaneous and triggered aseismic deformation transients in a subduction fault model. *Journal of Geophysical Research*, 112, B09404. <https://doi.org/10.1029/2007JB004930>

- Liu, Y., & Rubin, A. M. (2010). Role of fault gouge dilatancy on aseismic deformation transients. *Journal of Geophysical Research*, *115*, B10414. <https://doi.org/10.1029/2010JB007522>
- Liu, Y. J., & Rice, J. R. (2005). Aseismic slip transients emerge spontaneously in three-dimensional rate and state modeling of subduction earthquake sequences. *Journal of Geophysical Research*, *110*, B08307. <https://doi.org/10.1029/2004JB003424>
- Lowry, A. R., Larson, K. M., Kostoglodov, V., & Bilham, R. (2001). Transient fault slip in Guerrero, southern Mexico. *Geophysical Research Letters*, *28*(19), 3753–3756.
- Marone, C., & Kilgore, B. (1993). Scaling of the critical slip distance for seismic faulting with 1251 shear strain in fault zones. *Nature*, *362*, 618–622.
- Marone, C., Raleigh, C. B., & Scholz, C. H. (1990). Frictional behavior and constitutive modeling of simulated fault gouge. *Journal of Geophysical Research*, *95*, 7007–7025.
- Marone, C., & Saffer, D. (2015). The mechanics of frictional healing and slip instability during the seismic cycle. *Treatise on Geophysics*, *4*, 111–138. <https://doi.org/10.1016/B978-0-444-53802-4.00092-0>
- Marone, C., Vidale, J. E., & Ellsworth, W. (1995). Fault healing inferred from time dependent variations in source properties of repeating earthquakes. *Geophysical Research Letters*, *22*, 3095–3098.
- McLaskey, G. C., Thomas, A. M., Glazer, S. D., & Nadeau, R. M. (2012). Fault healing promotes high-frequency earthquakes in laboratory experiments and on natural faults. *Nature*, *491*, 101–105.
- Moore, D., Lockner, D., Shengli, M., Summers, R., & Byerlee, J. (1997). Strengths of serpentinite gouges at elevated temperatures. *Journal of Geophysical Research*, *102*(B7), 14,787–14,801.
- Nakatani, M. (1998). A new mechanism of slip-weakening and strength recovery of friction associated with the mechanical consolidation of gouge. *Journal of Geophysical Research*, *103*, 27,239–27,256.
- Nakatani, M. (2001). Conceptual and physical clarification of rate and state friction: Frictional sliding as a thermally activated rheology. *Journal of Geophysical Research*, *106*(B7), 13,347–13,380.
- Niemeijer, A., Marone, C., & Elsworth, D. (2008). Healing of simulated fault gouges aided by pressure solution: Results from rock analogue experiments. *Journal of Geophysical Research*, *113*, B04204. <https://doi.org/10.1029/2007JB005376>
- Niemeijer, A., Marone, C., & Elsworth, D. (2010). Frictional strength and strain weakening in simulated fault gouge: Competition between geometrical weakening and chemical strengthening. *Journal of Geophysical Research*, *115*, B10207. <https://doi.org/10.1029/2009JB000838>
- Niemeijer, A. R., Boulton, C., Toy, V. G., Townend, J., & Sutherland, R. (2016). Large-displacement, hydrothermal frictional properties of DFDP-1 fault rocks, Alpine Fault, New Zealand: Implications for deep rupture propagation. *Journal of Geophysical Research: Solid Earth*, *121*, 624–647. <https://doi.org/10.1002/2015JB012593>
- Niemeijer, A. R., & Spiers, C. J. (2005). Influence of phyllosilicates on fault strength in the brittle-ductile transition: Insights from rock analogue experiments. In D. Bruhn & L. Burlini (Eds.), *High-Strain Zones: Structure and Physical Properties*, Geological Society Special Publication, (Vol. 245, pp. 303–327).
- Niemeijer, A. R., & Spiers, C. J. (2007). A microphysical model for strong velocity weakening in phyllosilicate-bearing fault gouges. *Journal of Geophysical Research*, *112*, B10405. <https://doi.org/10.1029/2007JB005008>
- Niemeijer, A. R., Spiers, C. J., & Bos, B. (2002). Compaction creep of quartz sand at 400–600°C: Experimental evidence for dissolution-controlled pressure solution. *Earth and Planetary Science Letters*, *195*, 261–275.
- Noda, H., & Shimamoto, T. (2010). A rate- and state-dependent ductile flow law of polycrystalline halite under large shear strain and implications for transition to brittle deformation. *Geophysical Research Letters*, *37*, L09310. <https://doi.org/10.1029/2010GL042512>
- Paterson, M. S. (1995). A theory for granular flow accommodated by material transfer via an intergranular fluid. *Tectonophysics*, *245*, 135–151.
- Putelat, T., Dawes, J., & Willis, J. (2011). On the microphysical foundations of rate and state friction. *Journal of the Mechanics and Physics of Solids*, *59*, 1062–1075.
- Putelat, T., Dawes, J. H. P., & Willis, J. R. (2007). Sliding interactions of two frictional interfaces. *Journal of the Mechanics and Physics of Solids*, *55*(10), 2073–2105.
- Putelat, T., Dawes, J. H. P., & Willis, J. R. (2010). Regimes of frictional sliding of a spring-block system. *Journal of the Mechanics and Physics of Solids*, *58*, 27–53.
- Ranjith, K., & Rice, J. R. (1999). Stability of quasi-static slip in a single degree of freedom elastic system with rate and state dependent friction. *Journal of the Mechanics and Physics of Solids*, *47*, 1207–1218.
- Reinen, L. A., Tullis, T. E., & Weeks, J. D. (1992). Two-mechanism model for frictional sliding of serpentinite. *Geophysical Research Letters*, *19*(15), 1535–1538.
- Rice, J. R. (1983). Constitutive relations for fault slip and earthquake instabilities. *Pure and Applied Geophysics*, *121*, 443–475.
- Rice, J. R., Lapusta, N., & Ranjith, K. (2001). Rate and state dependent friction and the stability of sliding between elastically deformable solids. *Journal of the Mechanics and Physics of Solids*, *49*(9), 1865–1898.
- Rice, J. R., & Ruina, A. L. (1983). Stability of steady frictional slipping. *Journal of Applied Mechanics*, *50*, 343–349.
- Rice, J. R., & Tse, S. T. (1986). Dynamic motion of a single degree of freedom system following a rate and state dependent friction law. *Journal of Geophysical Research*, *91*, 521–530.
- Roy, M., & Marone, C. (1996). Earthquake nucleation on model faults with rate- and state-dependent friction: Effects of inertia. *Journal of Geophysical Research*, *101*(B6), 13,919–13,932.
- Rubin, A. M. (2011). Designer friction laws for bimodal slow slip propagation speeds. *Geochemistry, Geophysics, Geosystems*, *12*, Q04007. <https://doi.org/10.1029/2010GC003386>
- Ruina, A. (1983). Slip instability and state variable laws. *Journal of Geophysical Research*, *88*(B12), 10,359–10,370.
- Scholz, C. H. (2002). *The Mechanics of Earthquakes and Faulting* (p. 471). Cambridge, UK: Cambridge University Press.
- Schwartz, D. P., & Coppersmith, K. J. (1984). Fault behavior and characteristic earthquakes: Examples from the Wasatch and San Andreas fault zones. *Journal of Geophysical Research*, *89*, 5681–5698.
- Scuderi, M. M., Carpenter, B. M., Johnson, P. A., & Marone, C. (2015). Poromechanics of stick-slip frictional sliding and strength recovery on tectonic faults. *Journal of Geophysical Research: Solid Earth*, *120*, 6895–6912. <https://doi.org/10.1002/2015JB011983>
- Scuderi, M. M., Carpenter, B. M., & Marone, C. (2014). Physicochemical processes of frictional healing: Effects of water on stick-slip stress drop and friction of granular fault gouge. *Journal of Geophysical Research: Solid Earth*, *119*, 4090–4105. <https://doi.org/10.1002/2013JB010641>
- Segall, P., & Rice, J. R. (1995). Dilatancy, compaction, and slip instability of a fluid-infiltrated fault. *Journal of Geophysical Research*, *100*, 22,155–22,171.
- Segall, P., Rubin, A. M., Bradley, M., & Rice, J. R. (2010). Dilatant strengthening as a mechanism for slow slip events. *Journal of Geophysical Research*, *115*, B12305. <https://doi.org/10.1029/2010JB007449>
- Shibazaki, B., & Iio, Y. (2003). On the physical mechanism of silent slip events along the deeper part of the seismogenic zone. *Geophysical Research Letters*, *30*(9), 1489. <https://doi.org/10.1029/2003GL017047>

- Shibazaki, B., & Shimamoto, T. (2007). Modelling of short-interval silent slip events in deeper subduction interfaces considering the frictional properties at the unstable-stable transition regime. *Geophysical Journal International*, *171*(1), 191–205.
- Shimamoto, T. (1986). Transition between frictional slip and ductile flow for halite shear zones at room temperature. *Science*, *231*, 711–714.
- Sibson, R. H. (1990). Rupture nucleation on unfavorably oriented faults. *Bulletin of the Seismological Society of America*, *80*, 1580–1604.
- Sleep, N. H. (1995). Ductile creep, compaction, and rate and state dependent friction within major fault zones. *Journal of Geophysical Research*, *100*, 13,065–13,080.
- Sleep, N. H. (1997). Application of a unified rate and state friction theory to the mechanics of fault zones with strain localization. *Journal of Geophysical Research*, *102*(B2), 2875–2895.
- Spiers, C. J., De Meer, S., Niemeijer, A. R., & Zhang, X. (2004). Kinetics of rock deformation by pressure solution and the role of thin aqueous films. In S. Nakashima, et al. (Eds.), *Physicochemistry of Water in Geological and Biological Systems* (pp. 129–158). Tokyo: University Academic Press.
- Tse, S. T., & Rice, J. R. (1986). Crustal earthquake instability in relation to the depth variation of frictional slip properties. *Journal of Geophysical Research*, *91*, 9452–9472.
- Tullis, T. E., & Weeks, J. D. (1986). Constitutive behavior and stability of frictional sliding of granite. *Pure and Applied Geophysics*, *124*, 383–414.
- van den Ende, M., Chen, J., Ampuero, J. P., & Niemeijer, A. (2017). Earthquake and slow-slip nucleation investigated with a micro-physics based seismic cycle simulator. *Geophysical Research Abstracts*, *19*, EGU2017-7249
- Verberne, B. A., Spiers, C. J., Niemeijer, A. R., De Bresser, J. H. P., De Winter, D. A. M., & Plümper, O. (2013). Frictional properties and microstructure of calcite-rich fault gouges sheared at sub-seismic sliding velocities. *Pure and Applied Geophysics*, *171*, 2617–2640.
- Weeks, J. D., & Tullis, T. E. (1985). Frictional sliding of dolomite: A variation in constitutive behavior. *Journal of Geophysical Research*, *90*, 7821–7826.
- Wei, M., Kaneko, Y., Liu, Y., & McGuire, J. J. (2013). Episodic fault creep events in California controlled by shallow frictional heterogeneity. *Nature Geoscience*, *6*, 1–5.
- Wei, M., Liu, Y., Kaneko, Y., McGuire, J. J., & Bilham, R. (2015). Dynamic triggering of creep events in the Salton Trough, Southern California by regional $M \geq 5.4$ earthquakes constrained by geodetic observations and numerical simulations. *Earth and Planetary Science Letters*, *427*, 1–10.
- Wong, T.-f., & Zhao, Y. (1990). Effects of load point velocity on frictional instability behaviour. *Tectonophysics*, *175*, 177–195.
- Yasuhara, H., Marone, C., & Elsworth, D. (2005). Fault zone restrengthening and frictional healing: The role of pressure solution. *Journal of Geophysical Research*, *110*, B06310. <https://doi.org/10.1029/2004JB003327>
- Yoshida, S., & Kato, N. (2003). Episodic aseismic slip in a two-degree-of-freedom block-spring model. *Geophysical Research Letters*, *30*(13), 1681. <https://doi.org/10.1029/2003GL017439>